A Review of Deep-Learning-Based Approaches for Attenuation Correction in Positron Emission Tomography

Jae Sung Lee, *Senior Member, IEEE*

***Abstract*—Attenuation correction (AC) is essential for the generation of artifact-free and quantitatively accurate positron emission tomography (PET) images. PET AC based on computed tomography (CT) frequently results in artifacts in attenuation-corrected PET images, and these artifacts mainly originate from CT artifacts and PET-CT mismatches. The AC in PET combined with a magnetic resonance imaging (MRI) scanner (PET/MRI) is more complex than PET/CT, given that MR images do not provide direct information on high-energy photon attenuation. Deep-learning (DL)-based methods for the improvement of PET AC have received significant research attention as alternatives to conventional AC methods. Many DL studies were focused on the transformation of MR images into synthetic pseudo-CT or attenuation maps. Alternative approaches that are not dependent on the anatomical images (CT or MRI) can overcome the limitations related to current CT- and MRI-based ACs and allow for more accurate PET quantification in stand-alone PET scanners for the realization of low radiation doses. In this article, a review is presented on the limitations of the PET AC in current dual-modality PET/CT and PET/MRI scanners, in addition to the current status and progress of DL-based approaches, for the realization of improved performance of PET AC.**

***Index Terms*—Attenuation correction (AC), deep neural network, PET/MRI, positron emission tomography (PET).**

I. Introduction

MANY physical and patient factors influence the image quality and quantitative accuracy of ionizing radiation-based tomographic imaging techniques. If these factors are not properly considered and corrected, the quality and accuracy of tomographic images are degraded. In positron emission tomography (PET), which involves the collection of two high energy (511 keV) annihilation photons emitted from positron-emitting radioisotopes; photoelectric absorption and Compton scattering of high-energy annihilation photons are among the major physical factors that degrade the reconstructed images (Fig. 1) [1]. The photoelectric absorption and Compton scattering of the photons result in the loss of coincidence events (attenuation) in PET (Fig. 2). The effects of the photon attenuation are larger in PET than in single-photon emission computed tomography (SPECT), given that the loss of one of the two annihilation photons leads to the failure of coincidence event detection. However, the attenuation correction (AC) is straightforward in PET, given that the attenuation for the projection of coincidence events is independent of the position along the chord of projection (line of response) [2], [3].

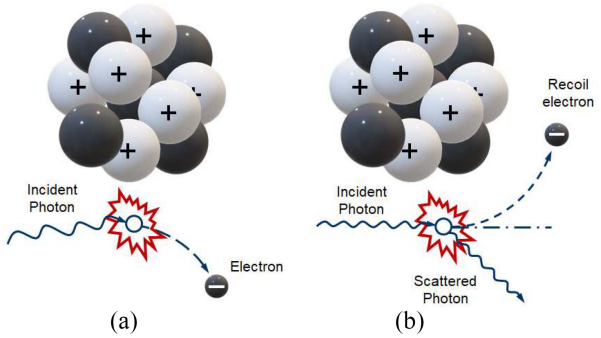

Fig. 1. Physics in PET attenuation: (a) photoelectric absorption and (b) Compton scattering.

Dual-modality hybrid PET systems require more accurate AC methods [4]. The quality of attenuation-corrected PET and SPECT images is significantly improved by combining them with X-ray computed tomography (CT) [5]–[7]. In the PET/CT, CT scans provide the linear attenuation coefficient map (μ-map: attenuation map for 511-keV photon) with better spatial resolution and higher counting statistics than conventional transmission PET scans [8]–[10]. However, the CT-based AC results in frequent artifacts in attenuation-corrected PET images. These artifacts, that mainly originate from CT artifacts and PET-CT mismatch, lead to errors in PET interpretation and quantification [11]–[15]. The AC in PET combined with a magnetic resonance imaging (MRI) scanner (PET/MRI) is more complex than PET/CT, given that magnetic resonance (MR) images do not provide direct information on high-energy photon attenuation [16]–[19]. Although various approaches have been proposed to overcome this drawback [20], issues remain to be solved in some applications.

Brain-dedicated stand-alone PET scanners require AC methods that do not use transmission data or other modality

Manuscript received April 2, 2020; revised July 2, 2020; accepted July 5, 2020. Date of publication July 17, 2020; date of current version March 3, 2021. This work was supported by the National Research Foundation of Korea (NRF) funded by the Korean Ministry of Science, ICT and Future Planning under Grant NRF-2016R1A2B3014645.

The author is with the Department of Nuclear Medicine, Seoul National University College of Medicine, Seoul 03080, South Korea, and also with the Department of Biomedical Sciences, Seoul National University College of Medicine, Seoul 03080, South Korea (e-mail: jaes@snu.ac.kr).

Color versions of one or more of the figures in this article are available online at https://ieeexplore.ieee.org.

Digital Object Identifier 10.1109/TRPMS.2020.3009269

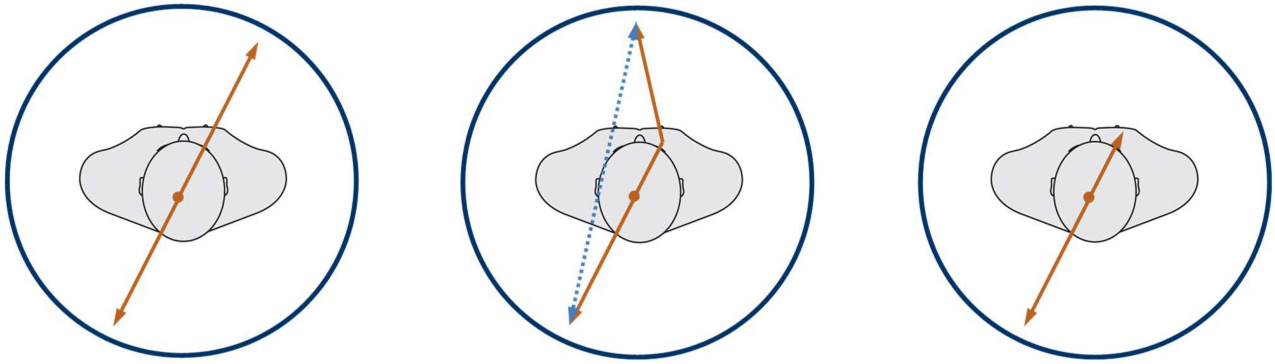

Fig. 2. Events in PET: (a) true coincidence, (b) scatter coincidence, and (c) loss of coincidence event due to photoelectric absorption.

images. Moreover, total-body PET/CT scanners exhibited issues related to the radiation exposure due to the CT part. With the aging of the global population, neurodegenerative disorders, such as Alzheimer's dementia and Parkinson's disease, have become a major health issue. PET allows for the highly sensitive and specific assessment of energy metabolic changes, amyloid plaque depositions, dopamine transporter losses, and many other pathologic changes in the brains of patients with neurodegenerative diseases. Therefore, various brain-dedicated PET scanners with different design concepts have been recently developed, most of which are stand-alone systems with no transmission sources or anatomical imaging modality combinations [21], [22]. A total-body PET scanner with a 2-m long axial field of view is creating new opportunities for clinical research and patient care [23], [24]. Given that the total-body scanner yields an approximately 40-fold sensitivity gain over existing PET scanners for the imaging of the entire body, it allows for PET scans to be conducted at extremely low radiation doses. However, an X-ray CT for AC and anatomical localization is required, thus limiting the low-dose capability of total-body PET [24].

With the advances of machine learning in medical imaging fields, various machine-learning approaches for the improvement of PET AC have been proposed [25]–[51]. Among these approaches, deep-learning (DL)-based methods have attracted significant research attention as alternatives to conventional AC methods. Many DL studies were focused on the transformation of MR images into a synthetic pseudo-CT or μ-map [34]–[44], [52]. Other approaches that are not dependent on the anatomical images (CT or MRI) can overcome limitations with respect to current CT- and MRI-based ACs and allow for more accurate PET quantification in stand-alone PET scanners for the realization of low radiation doses [25]–[33].

Therefore, this article provides a review on the following topics to provide the readers of IEEE TRANSACTIONS ON RADIATION AND PLASMA MEDICAL SCIENCES with the most up-to-date information on the PET AC technology.

1) The limitations of the PET AC in current dual-modality PET/CT and PET/MRI scanners, and the challenges in stand-alone organ-specific and total-body PET scanners.
2) Current status and progress of DL-based approaches for the realization of improved PET AC performances.

An assumption was made that the readers of this review paper are familiar with the fundamental physical principles of PET image acquisition and the reconstruction and correction processes in PET. Literature on the background of PET physics, reconstruction, and corrections are available elsewhere if required [3], [53]–[57]. In addition, the details of artificial neural networks (ANNs) and DL techniques are not presented, given the many available references [58]–[61].

In this article, Section II overviews the previous PET AC methods that use long-lived external radionuclides or body contours, and Section III summarizes the limitations of current CT-based AC. Section IV then overviews the state-of-the-art AC methods that are currently used for PET/MRI scanners. Each section describes the principles and limitations of each method. Section V presents the challenges in new emerging brain-dedicated stand-alone and total-body PET scanners, and Section VI describes the advances in simultaneous activity and attenuation reconstruction. In Section VII, previous artificial intelligence researches in nuclear medicine are summarized. Section VIII introduces recent DL-based approaches that are used for the transformation of diagnostic and nondiagnostic MR images into pseudo-CT or μ-map, and Section IX presents the DL-based AC methods that are not dependent on the anatomical images. Finally, in Section X, a scope for future research is provided.

II. CONVENTIONAL AC

A. Transmission PET

In the era of stand-alone PETs that were not combined with anatomical imaging modalities, a ring or rotating rod(s) of long-lived external radionuclides (^{68}Ga/^{68}Ge or ^{137}Cs) were used for the acquisition of the data required for the correction of the attenuation and scatter. Using the external radionuclides, transmission and blank scans were acquired, respectively, with and without objects (patients, phantoms, etc.) within the PET scanner (Fig. 3) [2], [3]. The ratio of the blank and transmission scans in the sinogram space provides AC factors (ACFs) used for the correction of the attenuation of annihilation photon pairs in the emission PET scan. The μ-map can be also

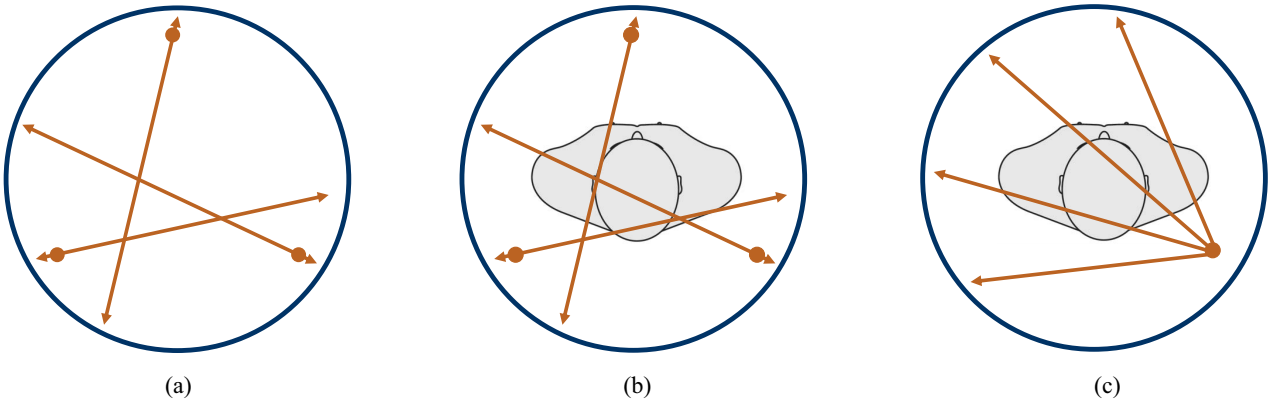

Fig. 3. AC using long-lived external radionuclides: (a) blank scan, (b) transmission scan with positron-emitting sources (^{68}Ge/^{68}Ga), and (c) transmission scan with a single-photon source (^{137}Cs).

reconstructed from the blank and transmission data. For the estimation and correction of scattered coincidences in the PET data, various empirical and analytical methods have been proposed [57]. Among them, the most commonly used method for modern clinical PET scanners is a single scatter simulation with tail-fitting scaling [62]–[65]. This method allows for an analytical estimation of the scatter contribution to projections, given the μ-map and the initial estimate of the scatter-free radioactivity distribution. These attenuation and scatter correction methods using the long-lived external radionuclides can significantly improve the quantitative accuracy of PET images. However, the main technical issues related to these methods are the extended scan time by the addition of the transmission scan and the increased noise in emission PET data due to the noise propagation from the noisy transmission scan [7].

B. Segmented and Calculated AC

Segmented and calculated ACs are alternative methods that provide noise-free μ-maps with reduced scan times. In the segmented AC, the measured μ-map derived from the transmission and blank scan data is segmented into several tissue types, and the known attenuation coefficient for each tissue type is assigned [66]. Although this method is useful for the reduction of the noise in attenuation-corrected PET images, there are several limitations, which include the susceptibility to the segmentation error and the variable tissue densities across the patients. The calculated AC was mainly used for brain PET studies [67], [68]. The head contour is extracted from uncorrected emission data, and the uniform attenuation coefficients for soft tissue and skull and constant skull thickness are assumed. Although this approach provides a noise-free μ-map and requires no transmission scan, a considerable activity bias in parietal and occipital lobes is the main limitation [69], [70].

III. CT-Based AC: Limitations

The X-ray CT data obtained using dual-modality PET/CT scanners has enhanced the confidence of PET findings by providing more accurate anatomical information. Moreover, the patient throughput and image quality of PET scans have been significantly improved by the use of CT data for PET AC, given that the CT scan is more rapid and yields less noise

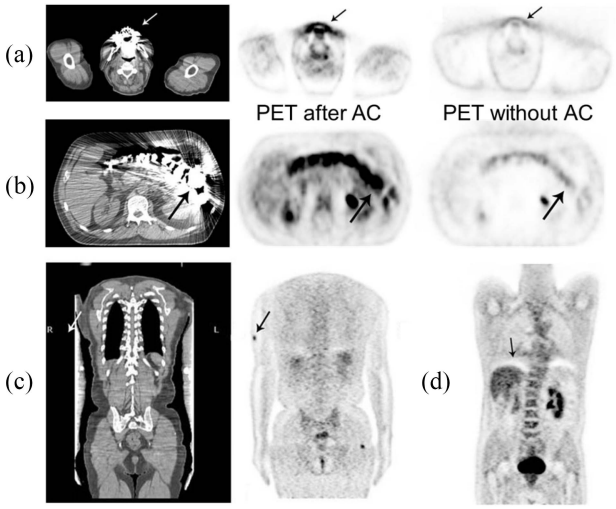

Fig. 4. Sources of imaging artifacts in PET/CT: (a) metal implants, (b) contrast medium, (c) body truncation, and (d) respiratory motion. (Reprint from [71] with permission; © 2005 SNMMI.)

than conventional transmission scans used in PET [5], [7]. Given that CT uses low-energy X-rays, the CT Hounsfield units must be converted into linear attenuation coefficients for photons with an energy of 511 keV usually using a bilinear relationship [7], [10]. Although the CT-based AC has several advantages over transmission scans with long-lived radionuclides, there are various error sources in CT-based AC (Fig. 4) [71].

1) Most artifacts shown in reconstructed CT images result in artifacts in attenuation-corrected PET images. The most common error source is the propagation of metal artifacts in CT due to the high-Z materials used in surgical and dental implants into the reconstructed PET images [Fig. 4(a)] [13], [14]. In general, regional PET activity around the high-Z materials is significantly overestimated [Fig. 4(b)].
2) CT generally has a smaller field of view than PET, thus leading to the truncation of the shoulders and arms of large patients in the CT images. Although these truncated body parts do not appear in the CT images, they cause attenuation in PET. These missing data in the

CT-based μ-map lead to the underestimated ACF and attenuation-corrected PET activity [Fig. 4(c)] [72], [73].

3) Given that X-ray photon flux in CT is significantly higher than the annihilation photon flux in PET, simultaneous PET/CT scans result in considerable cross-talk artifacts in PET images. Therefore, current PET/CT scanners are configured in a side-by-side tandem arrangement, thereby allowing for sequential CT and PET scans. Consequently, the movement of patients between the sequential CT and PET scans results in the misalignment of the PET and CT images and transmission-emission mismatch artifacts [74]–[76].
4) Artifacts due to spatial mismatches between PET and CT due to heartbeat and respiratory motions are common in CT-based attenuation-corrected PET images (e.g., banana-shape artifacts in the boundary between upper liver and lower lung, and artifactual defects in the myocardial PET) [Fig. 4(d)] [12], [15]. Although several different approaches have been proposed for the reduction of the misalignment artifacts based on a slow CT or a cine-CT [77], [78], the main drawback of these methods is increased radiation transmitted to the patients.

IV. AC IN PET/MRI

It should be noted that PET/MRI has several advantages over PET/CT, which include a smaller amount of radiation transmitted to the patients and improved contrast between different soft tissues [5], [18], [79]–[82]. In addition, MRI allows for the multiparametric assessment of pathologic tissues based on many different MRI pulse sequences. Besides the anatomical assessment based on the most conventional $T1$ and $T2$ contrast imaging method, various functional and physiological processes (i.e., perfusion and diffusion) can be captured using MRI. Therefore, the advantages of PET/MRI have been clarified in various diagnostic procedures, which include head, neck, prostate, breast, musculoskeletal, and neuroendocrine tumor imaging [19], [83]–[88]. Moreover, the advances in semiconductor photosensors, such as avalanche photodiodes and silicon photomultipliers, have allowed for simultaneous PET/MR imaging [80], [81], [89]–[93]. This simultaneous PET/MRI scan allows for an improved spatiotemporal correlation between two modalities when compared with PET/CT, in addition to motion correction in PET based on motion information derived from MRI [94]–[97].

However, accurate PET attenuation and scatter corrections are limited in PET/MRI. The image intensity of MRI and CT (or transmission PET) is determined by different physical principles. For example, their image intensities are mainly dependent on the proton and electron densities, respectively. Moreover, the MR image contrast is determined by the different relaxation times of the MR-active nuclei in different molecules and environments. In contrast, the amount of high-energy photon attenuation is measured in CT or transmission PET scans. There is currently no direct MR estimation method for such a high-energy photon attenuation. Hence, several indirect approaches are employed in PET/MRI [16], [18]–[20], [98]. However, the accuracy of these AC methods has been proven to be within acceptable quantitative limits only in the adult brains with normal anatomy [20].

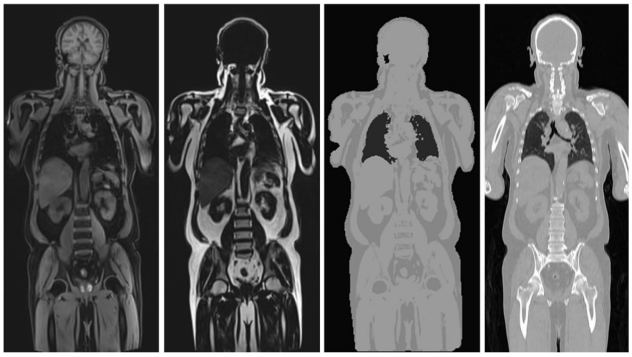

Fig. 5. Dixon MRI-based AC: (a) Dixon water image, (b) Dixon fat image, (c) attenuation map generated by combining the water and fat images, and (d) CT scan of the same patient. (Reprint from [19] according to the publisher's open access policy.)

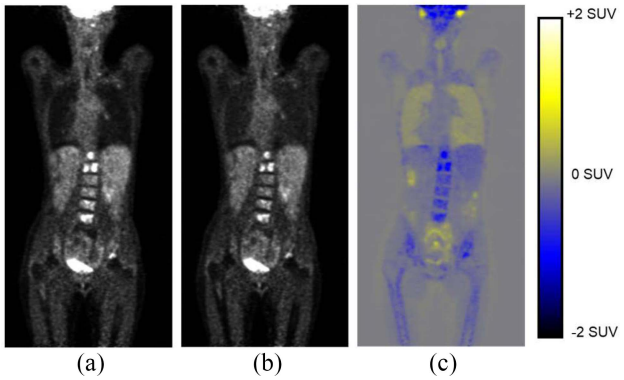

Fig. 6. Difference between AC methods: (a) CT-based AC, (b) Dixon MRI-based four-segment method, and (c) difference between (a) and (b).

A. Dixon MRI-Based

In current clinical PET/MRI scanners, μ-map generation for body PET/MRI scans is mainly based on the Dixon MRI pulse sequence [99]–[101]. The Dixon MRI exploits the different precession rates of proton spins in water and fat molecules [102]. Therefore, they are alternatively in-phase and out-of-phase. From the simultaneously obtained in-phase and out-of-phase images, water-only and fat-only images can be generated. By assigning predetermined attenuation coefficients to the fat- and water-equivalent tissues and segmented lung regions, a four-segment (background, lungs, fat, and water) μ-map is generated (Fig. 5) [101]. The difference between attenuation-corrected PET images using CT-based and Dixon MRI-based μ-maps is dependent on the location of lesions. The variation of the lung attenuation coefficient for different patients is large [103]–[106], and the liver has a higher attenuation coefficient than other water segments [107]. Given that the contribution of bone to the 511-keV photon attenuation is not considered in the Dixon MRI-based AC, the

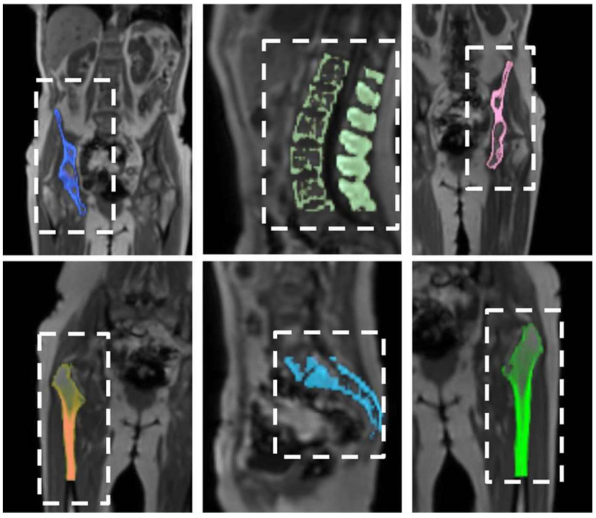

Fig. 7. Local bone masks employed for a model-based AC method in PET/MRI. (Reprint from [110] with permission; © 2015 SNMMI.)

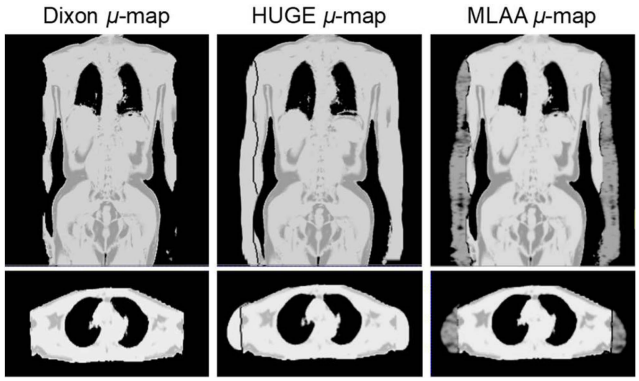

Fig. 8. HUGE: an MRI-based truncation correction method.

difference is largest in osseous lesions where the PET activity is considerably underestimated (Fig. 6) [101], [107]–[109]. To overcome the above-mentioned limitations of the Dixon MRI-based four-segment method, a model-based approach was proposed [110], [111]. In the model-based approach, bone structures are added to four-segment maps using bone templates and image registration (Fig. 7). However, the inaccurate registration between PET images and bone models can lead to errors in PET activity quantification [28].

The smaller field of view of MRI when compared with PET can cause truncation artifacts in PET AC. For example, the arms of the patients are not completely covered by MRI when the patients are scanned with their arms hanging downward. The arm truncation in the MRI-based μ-map of whole-body PET/MRI scans leads to a considerable bias in PET activity quantification [112]. The missing parts in the MRI can be estimated from the nonattenuation-corrected (NAC) PET. Alternatively, the μ-map for missing parts can be derived using the maximum-likelihood reconstruction of activity and attenuation (MLAA) algorithm [113], which is a simultaneous activity and attenuation reconstruction algorithm. However, the MLAA-based approach frequently yields overestimated arm volumes and associated artifacts. Similarly, the MLAA enables the estimation of other missing parts in the μ-map, such as flexible MRI coils and metal implants [114], [115]. The MLAA can be further improved in the case where the time of flight (TOF) is known as in recent PET/MRI scanners. HUGE (*B*0 homogenization using gradient enhancement) is a fully MR-based truncation compensation method that determines an optimal readout gradient for the compensation of gradient nonlinearities at the peripheral MR field of view (Fig. 8) [116]. The HUGE exhibited an improvement in the μ-map generation and PET quantification; however, it requires additional MRI scans to cover both arms.

B. UTE

For brain PET/MRI studies, the contribution of the skull to the annihilation photon attenuation is high relative to the soft tissues. Therefore, two different approaches are mainly used for the generation of PET μ-maps that include bone. The derivation of PET μ-maps from the ultrashort echo time (UTE) [99], [117]–[125] or zero echo time (ZTE) MR images [126]–[131] is one of the two approaches. In these methods, patient-specific bone information is captured from the MR images of the patient, and discrete or continuous bone attenuation coefficient values are estimated. The UTE and ZTE pulse sequences that commonly use radial *k*-space sampling and fast switching between transmitting and receiving radiofrequency (RF) pulses depict bones based on $T2^*$-weighting and proton-density-weighting, respectively [132]. Given that the proton density is low (approximately 20% of water) and $T2$ relaxation occurs rapidly (approximately 390 μs at 3.0 T) in cortical bone tissues [133]; the bone signal is low in conventional MR images (e.g., $T1$ and $T2$), and bone structures cannot be distinguished from the air. In the UTE sequence employed in the Siemens mMR PET/MRI scanner (Siemens Healthineers, Knoxville, TN, USA), the first echo [MR signal observed following excitation pulse(s)] is sampled at maximum speed (70–150 μs) after the excitation, and the second echo is sampled as in the conventional MRI sequences ($\geq$ 1 ms) [121], [123]. By the subtraction/division of the second long echo-time image from/by the first ultrashort echo-time image, the bone and soft tissue can be distinguished (Fig. 9) [99], [120], [121], [123], [125].

However, these images, especially the second longer echo-time image, are sensitive to off-resonance effects owing to B_0 inhomogeneity and susceptibility. The off-resonance effects result in inhomogeneity artifacts that can lead to inaccurate image segmentation and bone delineation [134]. In addition, the UTE images are subject to eddy-current artifacts, given that UTE sequences require samples to be acquired during rapidly changing gradient fields [118]. Therefore, frequent segmentation errors were observed at the boundaries between soft tissue, bone, and air in the initial versions of the UTE-based μ-maps [119], [121], [135], [136]. Moreover, there were instances wherein the ventricles in the brain were misclassified as air [135].

Some methods have been proposed for the improvement of the UTE-based AC. Aitken *et al.* [118] measured true *k*-space trajectories during a dual-echo UTE sequence using

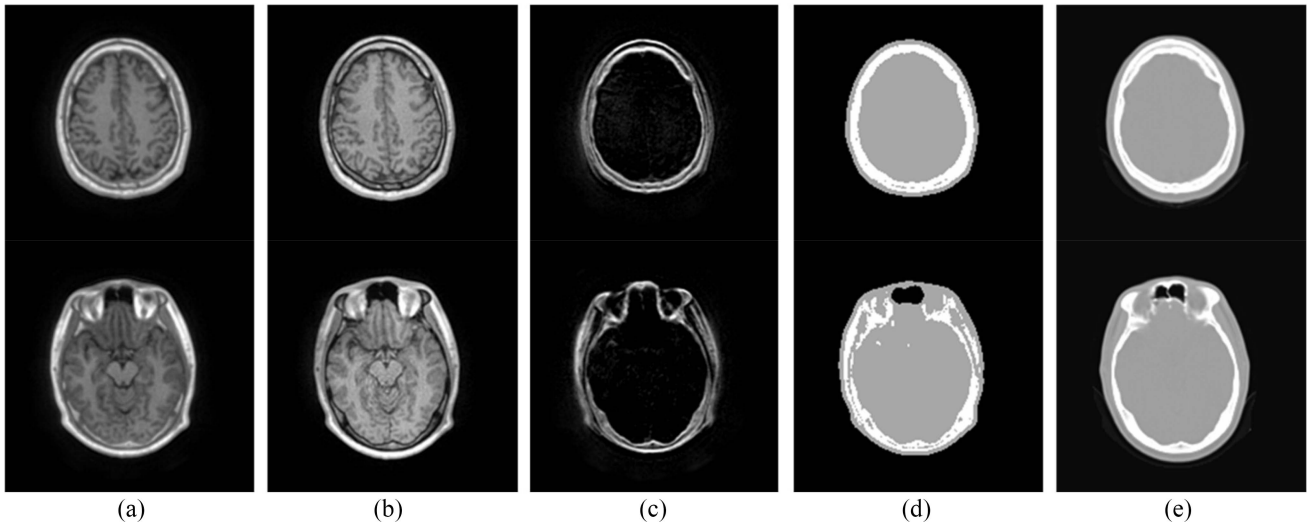

Fig. 9. UTE MRI-based AC: (a) first echo [echo time (TE) = 0.7 ms], (b) second echo (TE = 2.46 ms), (c) difference between (a) and (b), (d) UTE-based μ-map, and (e) CT of the same patient. (Reprint from [19] according to the publisher's open access policy.)

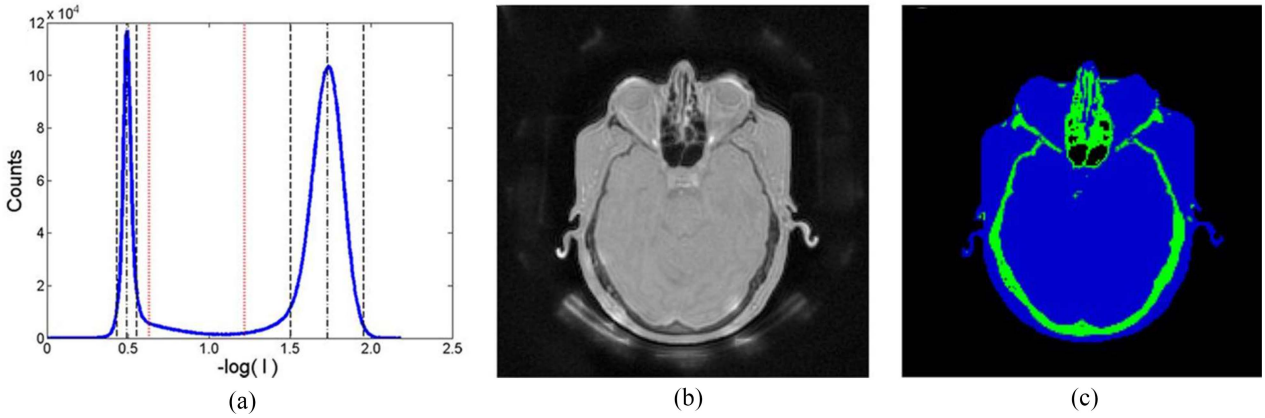

Fig. 10. ZTE MRI-based AC: (a) intensity histogram of ZTE MRI after logarithmic rescaling, (b) ZTE MRI, and (c) soft tissue (blue) and bone mask (green) obtained with segmentation. (Reprint from [127] with permission; © 2015 SNMMI.)

a dynamic magnetic field camera and obtained reconstructed UTE images using the measured trajectories to compensate for the eddy-current artifacts in UTE images. In this method, a one-time calibration scan is required, and the measured trajectories can be used in all subsequent image reconstructions for the same set of scan parameters. An *et al.* improved the UTE-based AC by the application of a multiphase level-set algorithm for the UTE MRI segmentation, in which the intensity inhomogeneity correction was incorporated. The PET quantification error was reduced by a factor of 3 by the application of the level-set segmentation to the UTE MR images [119]. Several methods were proposed for the association of the MR relaxation time R_2* and CT Hounsfield unit to provide continuous-valued attenuation coefficients for bone [122], [124]. A combination of UTE with Dixon MRI or atlas-based segmentation is an alternative approach for the improvement of UTE-based μ-map generation [99]. Despite continuous improvements in the UTE-based method, segmentation errors are observed, especially with respect to neck or face/nasal regions [117], [119].

C. ZTE

The ZTE pulse sequence also provides enhanced bone contrast in MR images. In the ZTE MRI, the signal is obtained immediately after the RF excitation, thus allowing for the contrast from the proton-density difference to be determined [137]. The ZTE does not require long $T2$ suppression methods such as the echo subtraction used in UTE; thus, ZTE has a superior signal-to-noise ratio and scan time efficiency than UTE [138]. In addition, ZTE is robust against off-resonance effects and gradient system imperfections [132]. In the ZTE-based μ-map available in the GE SIGNA PET/MRI scanner (GE Healthcare, Chicago, IL, USA), bone and tissue masks are derived from reconstructed ZTE images by the application of bias correction and intensity normalization, followed by a histogram-based thresholding operation and piecewise linear intensity mapping [126], [127], [130], [139]. Based on two thresholds, the images are segmented into three classes, namely, soft tissue, bone, and air, given that the bone has a distinct intensity between the soft tissue and air peaks in the intensity histogram of the ZTE MRI (Fig. 10).

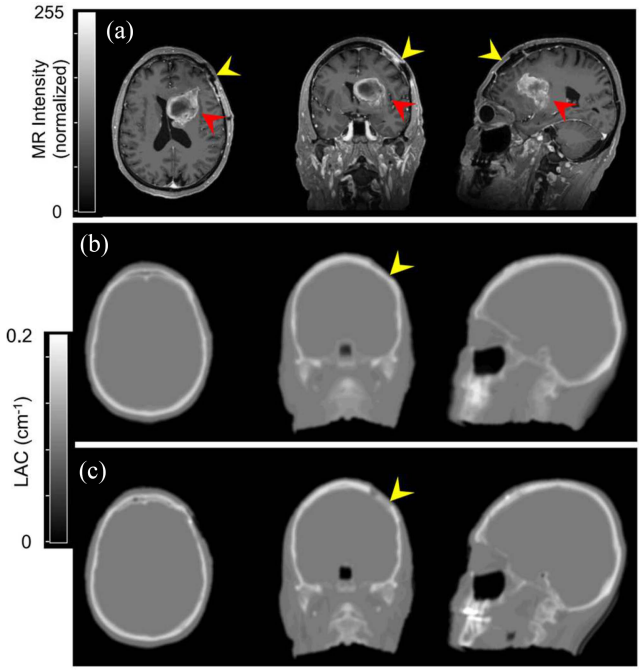

Fig. 11. Combination of atlas-based and segmentation-based method: a challenging case showing a large tumor in the ventricles and skull thickness change after the surgical procedure. (a) MRI, (b) atlas/segmentation-based μ-map, and (c) CT-based μ-map. (Reprint from [143] with permission; © 2014 SNMMI.)

The main drawback with respect to the ZTE-based AC method is the misclassification of the regions with air/tissue/bone mixtures (e.g., nasal sinus cavity and temporal bones) or their interfaces as bone [129], [131]. The PET quantification error due to this misclassification in the skull base can be reduced by the application of a sinus–edge-correction method, in which the sinus and edge masks are generated for removal of the false-positive bone pixels [131]. In addition, the ZTE-based method with the improved segmentation in the sinus and temporal bones [126] exhibited a superior performance to the atlas-based method in a comparative brain ^{18}F-fluorodeoxyglucose (^{18}F-FDG) PET/MRI study with a relatively large number of subjects [129].

Furthermore, a limited number of studies have been conducted for the application of the ZTE MRI to body parts apart from the brain. A hybrid method was proposed by Leynes *et al.*, who combined the ZTE and Dixon MRI information for the generation of pseudo-CT images in pelvic regions. In this method, a continuous two-segment piecewise linear model is used to convert the ZTE MR image intensity in bone into Hounsfield units [128].

D. Atlas-Based

An alternative approach used in brain PET/MRI is the atlas-based AC method [45], [47], [140]–[148]. A single atlas-based method is used for GE SIGNA PET/MRI scanners [147]. In this method, a single head atlas generated from multiple head CT images is registered with a bone-enhanced LAVA-Flex (two-point Dixon sequence in GE SIGNA PET/MRI scanner) in-phase MR image. The registered head CT atlas is combined with a head contour derived from the MR image for the generation of a μ-map. Given that the LAVA-Flex MRI sequence is short and only a single nonlinear image registration is carried out, this relatively simple approach allows for a more efficient PET/MRI workflow [147]. Alternatively, an atlas that consists of a CT and MRI pair (single or average) can be utilized. For a new given subject, the MRI atlas is registered with the MR image of the new subject, and the same registration parameters are applied to the CT atlas to be transformed to the subject-specific pseudo-CT [47], [144], [146]. The atlas-based methods are less sensitive to the MRI acquisition artifacts than segmentation-based approaches.

However, the main limitation of the single atlas-based method is the error due to the residual misregistration, which can be mainly attributed to interpatient anatomic variations [19], [99]. In general, it is not suitable for patients after surgery and those with implants. The solutions to the drawbacks of the single atlas-based method include the combination of atlas-based and segmentation-based methods [45], [47], [142], [143] (Fig. 11) and the use of multiple atlases [141], [145], [148]. In the multiatlas-based approaches, the regional intensity distribution of the pseudo-CT is optimized by applying a weighted average of multiple pseudo-CT images derived from a large dataset of CT and MRI atlas pairs, thus reducing the error in the PET AC due to incomplete registration and patient variability; which, however, increases the computational time (Fig. 12). Although the atlas-based approaches exhibited suitable performances in the brain PET/MRI studies, with the exception of postoperative patients and patients with implants, the application of the atlas-based approaches to the entire-body PET/MRI studies is still challenging due to their limitations with respect to the significant anatomical variations of the organs in the chest and abdomen, especially in cancer patients.

E. AC for RF Coils

Although MR RF coils cause significant attenuation of PET photons, they are not typically visible in MR images. The attenuation by rigid coils, such as the head and spine coils, in addition to the patient table, is corrected by the addition of the CT-based μ-map of these components to the patient μ-map. However, the AC for flexible coils is not conducted in commercial PET/MRI scanners although PET quantification errors up to 20% are yielded [149]–[151]. There is a modified MLAA algorithm proposed to estimate the attenuation of flexible coils and other hardware components [115]. A detailed review on the AC for MR coils in PET/MRI can be found in [149].

V. New Emerging PET Scanners

A. Brain-Dedicated PET

With the aging of the global population, neurodegenerative diseases, such as Alzheimer's disease and Parkinson's disease, have become more common. Moreover, PET is a useful clinical tool for the accurate visualization of the biomarker present in the brain related to various neurodegenerative diseases (e.g., amyloid-β plaques or strands of microtubule-associated protein tau) [152]–[155]. However, a relatively high level of

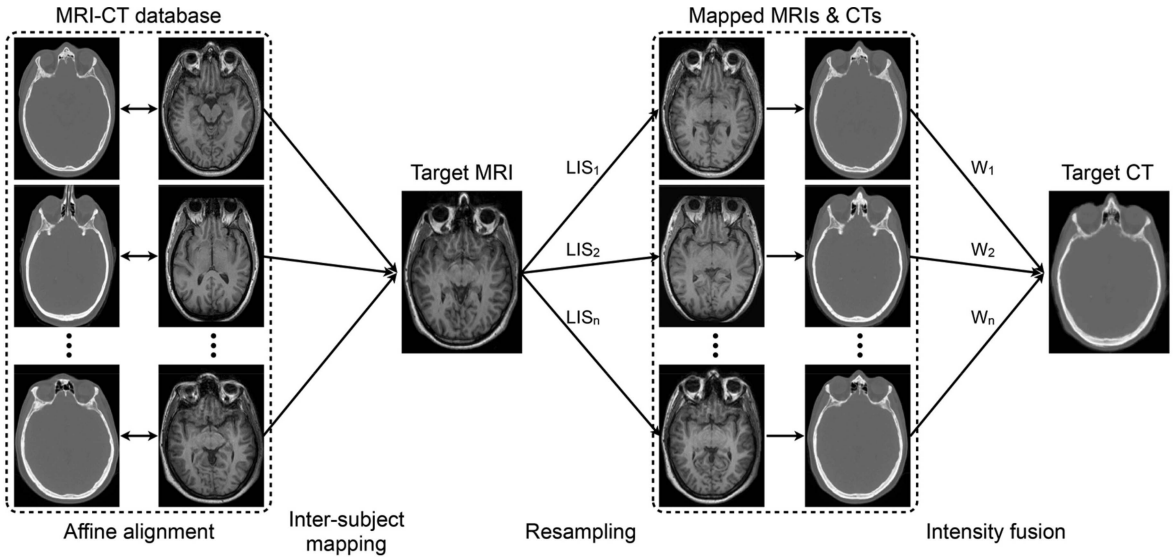

Fig. 12. Multiple atlas-based AC. (Reprint from [141] with permission; © 2014 IEEE.)

radiation exposure and a long scan time, in addition to the high costs of hybrid PET/CT and PET/MRI scans, are the main drawbacks of current PET examinations. For the solution of these drawbacks, many brain-dedicated stand-alone PET scanners have been developed, such as helmet-type or wearable PET scanners used on seated patients [21], [156]–[159] [Fig. 13(a)].

As previously mentioned, a major technical limitation to brain-dedicated stand-alone PET scanners is the lack of physically measured μ-maps for attenuation and scatter corrections. The calculated AC based on predetermined attenuation coefficients for soft tissue and bone is a simple solution for brain-dedicated PET scanners [67], [68]. However, the accuracy of the calculated AC is limited by the nonuniformity of tissue compositions owing to pathologic conditions and the complex structure of facial bones. Moreover, the calculated AC generally leads to the underestimation of the brain PET intensities in frontal and occipital lobes [69], [70]. Although the atlas-based AC method is an alternative solution, it exhibits similar drawbacks, as previously described [131].

B. Total Body PET/CT

The low-dose capacity of total-body PET/CT is limited by the CT radiation dose. A major factor that determines the physical sensitivity of the PET scanner is the axial length. By the increase of the axial length from 20 cm to 2 m in total-body PET, the effective sensitivity of the PET scan is increased by 40-fold [23]. For the same scan time and counting statistics, the radiation dose in the PET scan can be remarkably reduced [Fig. 13(b)]. However, the radiation dose from the CT scan that still needs for anatomical localization and AC is considerably high [24]. The CT dose reduction based on deep neural networks has attracted significant research attention in the medical imaging field [160]–[162], especially with respect to effective dose reduction in the total body PET/CT.

In the applications that do not require detailed anatomical information provided by CT, emission-only approaches, as described in the following sections, are effective for the realization of extremely low-dose studies. In particular, the DL-based conversion of NAC PET to attenuation-corrected PET [29]–[33], in addition to the DL-enhanced simultaneous activity and attenuation reconstruction [25]–[28], are suitable.

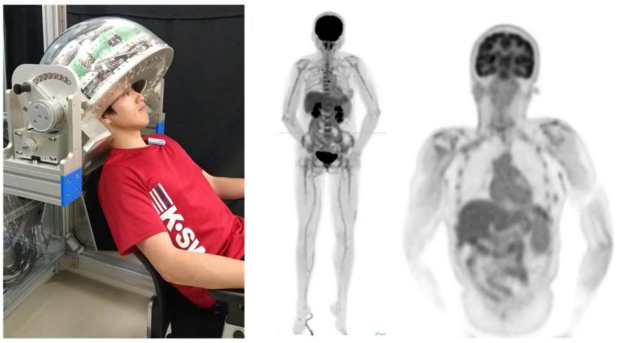

(a) (b)

Fig. 13. New emerging PET scanners: (a) brain dedicated PET scanner without CT, (b) low-dose imaging with total body PET (10-min scan obtained 52.5 min after the intravenous injection of 25 MBq ^{18}F-FDG.) (Reprint from [23] and [156] with permission; © 2019 SNMMI and IPEM.)

VI. Simultaneous Activity and Attenuation Reconstruction

A potential solution to the above-mentioned drawbacks related to PET/CT and PET/MRI, in addition to stand-alone brain PET and total-body PET, is simultaneous activity and attenuation reconstruction. However, the performance of the current simultaneous activity and attenuation reconstruction algorithms is dependent on the timing resolution of the PET scanner.

The application of spatial constraints to the uncertainty of the event location in PET activity reconstruction by the use of the TOF information allows for an increase in the effective sensitivity of the PET system and improvement of signal-to-noise ratio [163], [164]. The effective gain in the sensitivity,

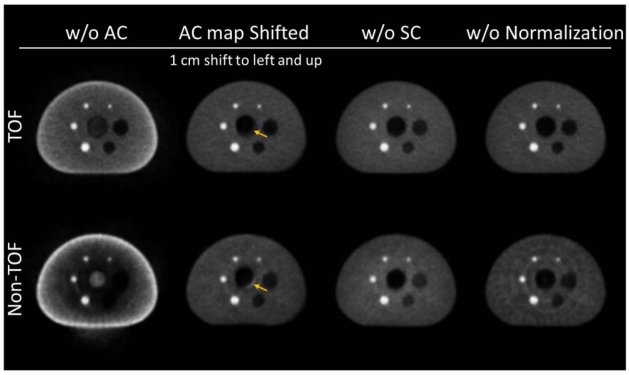

Fig. 14. Robustness of TOF PET to the errors in data correction (phantom images reconstructed without the application of the physical correction factors). (Reprint from [168] with permission; © 2017 AAPM.)

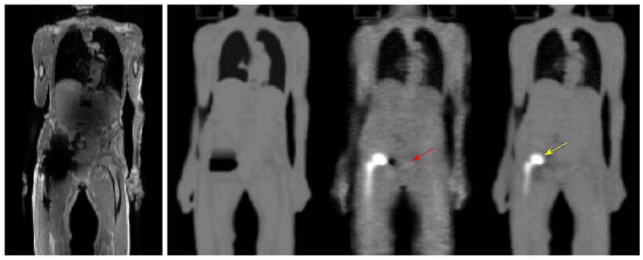

Fig. 15. Joint estimation of activity and attenuation using MRI-based prior: (a) Dixon in-phase MRI, (b) Dixon MRI-based μ-map, (c) MLAA μ-map without MRI-based prior, and (d) MLAA μ-map with MRI-based prior. (Reprint from [179] with permission; © 2018 IPEM.)

which is dependent on the patient size and system timing resolution, allows for the improvement of the diagnostic accuracy of PET and/or the reduction of the scan time or radiation dose [165]. The TOF information is effective for the reduction of the PET image artifact or quantification error due to inconsistent or missing data in PET measurements. This is because the TOF information allows for a more accurate determination of the annihilation event location in the line of response [166], [167]. Therefore, the images of the PET systems with precise timing resolution are influenced less by photon attenuation and Compton scattering. In addition, the TOF PET systems yield fewer artifacts due to the misalignment of emission and transmission data in AC than non-TOF PET systems (Fig. 14) [168], [169].

The information on the spatial origin of annihilation photons provided by TOF measurement allows for the distinction of events due to the radiotracer within the body from those due to external transmission sources. Simultaneous emission and transmission scans with external transmission sources based on the TOF information were proposed to overcome the limitations of the current AC methods in PET/MRI [170]. Moreover, the natural background radioactivity present in the lutetium-based scintillators used in PET scanners can be discriminated from the emission events based on TOF information. Upon the decay of ^{176}L due to beta emission with prompt cascading gamma rays with the energies of 307, 202, and 88 keV; a transmission scan can be obtained by using 307 and 202 keV gamma rays simultaneously with an emission PET scan [171].

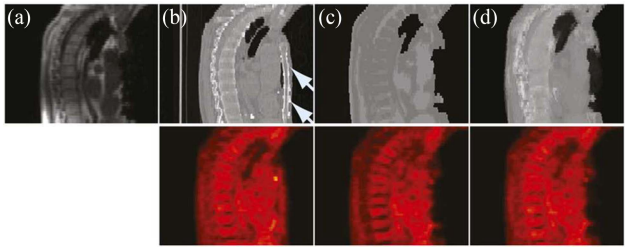

Fig. 16. Combined atlas-based AC and pattern recognition: (a) Dixon in-phase MRI, (b) CT-based AC, (c) Dixon MRI-based AC, and (d) combination of atlas and pattern recognition. Upper row: μ-maps. Bottom row: corresponding emission images. (Reprint from [108]; © 2011 SNMMI.)

The TOF information allows for a more accurate simultaneous reconstruction (or joint estimation) of the activity and attenuation based only on the attenuated emission dataset [172]–[175]. As demonstrated theoretically and experimentally, the solution of simultaneous reconstruction is determined up to a constant based on available TOF information [173]. An effective method for simultaneous reconstruction is the previously mentioned MLAA algorithm. In the MLAA, activity and attenuation images are updated by the alternate application of the maximum-likelihood expectation–maximization and maximum-likelihood transmission tomography equations [174]. Given that the μ-map is provided with the activity image, image-domain priors for the improvement of the accuracy and convergence of the algorithm (e.g., zero attenuation outside body contour and known attenuation in some body parts) can be applied [166], [174]. However, due to the insufficient timing resolution of current clinical PET systems, the MLAA is subject to slow convergence, the high noise level in the μ-map, and the crosstalk between the activity and attenuation distribution [172]. Another approach to the simultaneous activity and attenuation reconstruction is the maximum-likelihood ACF (MLACF) [176], [177]. Given that the MLACF allows for the determination of the ACF without the reconstruction of the μ-map, the convergence rate is higher and the computation complexity is lower than those of the MLAA. However, the knowledge of the total prior activity is necessary for MLACF to determine the constant scaling, given that no image-domain prior can be applied. In addition, a scatter estimate of the emission measurement should be assumed in the joint estimation algorithms [178].

Several methods have been proposed for the improvement of the MLAA algorithm [178]–[180]. For example, a Gaussian mixture model was employed in the attenuation estimation to utilize the prior knowledge that the histogram of the attenuation values generally consists of several distinct peaks corresponding to fat, soft tissue, and bone [180]. In this approach, spatial information derived from the Dixon MR images was incorporated into the Gaussian mixture model for the enhancement of known tissue types, thereby leading to the considerable suppression of noise and crosstalk. Ahn *et al.* [179] proposed another approach for the exploitation of the synergies between the MLAA- and Dixon-based AC (Fig. 15). In this method, the weight of the Dixon MRI-based prior used in the MLAA framework was modulated based on

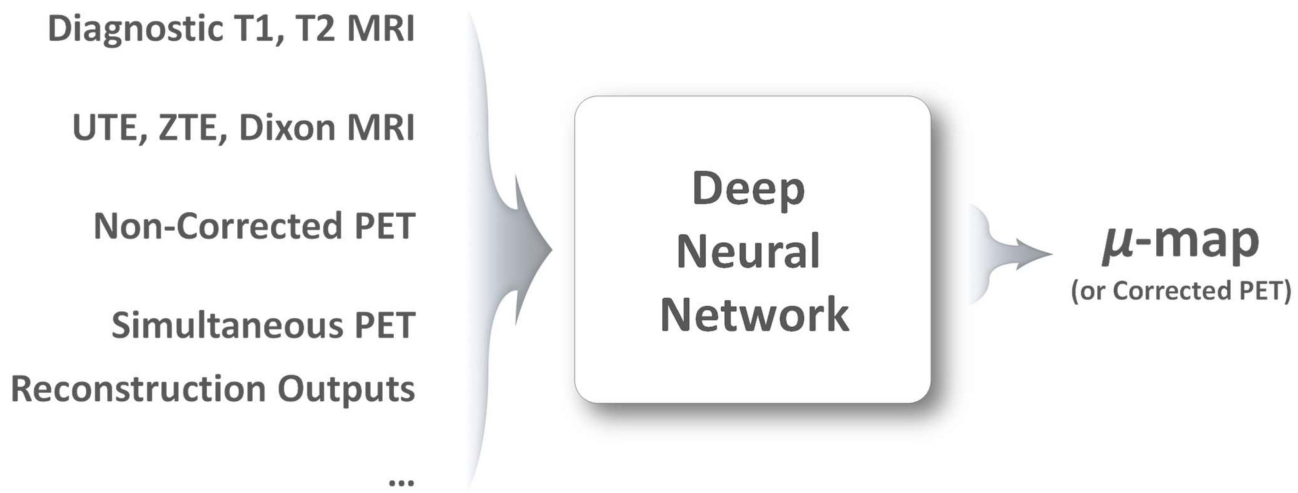

Fig. 17. Different DL-based approaches for PET AC.

the MR signal strength. In the regions with strong MR signals, such as those of soft tissue and fat, large prior weights were applied. Conversely, a small weight is assigned to the regions where the MR signal was low and the tissue class cannot be clearly distinguished, which may include bones, internal air, metallic implants, and lungs; thus allowing for the estimation of attenuation coefficients in these regions based on the MLAA. Recently, iterative methods that estimate the scatter distribution during the MLAA reconstruction accelerated using an ordered subset were proposed as more practical solutions for PET AC [166], [178].

VII. Artificial Intelligence in Nuclear Medicine

Artificial intelligence and machine learning are two of the most widely investigated mathematical and engineering techniques in the biomedical engineering field [181]–[187]. In recent decades, various techniques based on artificial intelligence and machine learning have been applied to nuclear medicine images. For a more accurate determination of the annihilation photon interaction position in the scintillation crystal array in the PET detector block, position decoding methods based on ANNs have been proposed [188], [189]. Data-driven approaches such as blind source separation techniques based on unsupervised neural networks have been extensively researched for the extraction of different physiological components (e.g., arterial input function for kinetic modeling) from dynamic PET scans [190]–[193]. In addition, various machine learning techniques have been applied to myocardial perfusion SPECT images for the identification of the perfusion defects and location, in addition to the improvement of the diagnostic and prognostic accuracies [194].

Moreover, attempts were initially made to utilize the ANNs for the improvement of the AC in nuclear medicine images [48]–[51]. Yu *et al.* used an ANN that involves a principal component analysis and multilayer perceptron for the improvement of the segmented AC. The input to the ANN was the local matrix with 7×7 pixels of the measured μ-map, as obtained using transmission data over a period of 5 min, and the outputs were the conditional probabilities that the center pixel of the matrix was related to the three different tissue classes (air, lung, and soft tissue) [48]. The desired output of the ANN for each pixel was assigned based on the segmented attenuation map obtained using transmission data over a period of 3 h. The trained ANN yielded superior μ-maps and corresponding emission images than the measured AC. In addition, there was no significant difference between the qualities of the images based on transmission data over periods of 5 and 25 min with the application of the ANN-based segmented AC method. The scatter estimation from five energy windows was estimated using an ANN by Ogawa and Nishizaki [49]. Moreover, ANN-based simultaneous scatter and attenuation compensation in SPECT and planar scans were also attempted [50], [51].

Hofmann *et al.* [46], [47] recently proposed an MR-based AC method that combined atlas-based AC and pattern recognition using a registered atlas as prior knowledge. In this approach, nonrigid registration is conducted between MRI/CT pairs in the atlas database and the new MR image of the subject, and all the neighboring MR patches are found in the registered database to perform Gaussian process regression on patch and position to yield a CT estimate for every pixel. This approach allows for the PET quantification with a mean error of 3.2% in the brain and 7.7% in whole-body PET images. However, the error was high in the thorax region (14.0%), and in patient with metal implants (Fig. 16). Ribeiro *et al.* [45] combined atlas-based and UTE MRI-based AC methods using a feedforward neural network. In this method, neighboring pixel values in a registered CT atlas and UTE MR images were inputted into the neural network to yield an estimated CT value for each pixel. In the bone region of the head, the ANN-based approach exhibited a higher Dice similarity (0.77) than the atlas-based method (0.51).

In most areas of nuclear medicine, DL-based image processing and analysis techniques have received significant research attention [184], [195], [196]; namely, the DL-based image reconstruction and denoising for radiation dose reduction [197]–[200], automatic segmentation of various organs

TABLE I
DL-BASED APPROACHES FOR PET AC

Approach	Reference	Input	Output	Network	Region	PET tracer
Diagnostic MRI to Pseudo-CT	Nie [40]	T1 MRI	Pseudo-CT	FCN	Pelvis	Not used
	Nie [39]	T1 MRI	Pseudo-CT	GAN	Brain/Pelvis	Not used
	Han [42]	T1 MRI	Pseudo-CT	U-net	Brain	Not used
	Bradshaw [43]	T1, T2 MRI	Pseudo-CT	Multi-scale CNN	Pelvis	^{18}F-FDG
	Liu [41]	T1 MRI	Pseudo-CT	CAE	Brain	^{18}F-FDG
	Spuhler [38]	T1 MRI	CT μ-map	U-net	Brain	^{11}C-WAY-100635 ^{11}C-DASB
	Arabi [44]	T1 MRI	Pseudo-CT	GAN	Brain	^{18}F-FDG
Non-diagnostic MRI to Pseudo-CT	Jang [37]	UTE MRI	Pseudo-CT	CED	Brain	^{18}F-FDG
	Ladefoged [36]	UTE MRI	Pseudo-CT	U-net	Brain	^{18}F-FET
	Leynes [35]	ZTE, Dixon MRI	Pseudo-CT	U-net	Pelvis	^{18}F-FDG ^{68}Ga-PSMA-11
	Torrado-Carvajal [34]	Dixon MRI	Pseudo-CT	U-net	Pelvis	^{18}F-FDG ^{18}F-choline
	Gong [224]	Dixon MRI	Pseudo-CT	CycleGAN	Brain	^{18}F-FDG
NAC PET to Pseudo CT	Liu [30]	NAC PET	Pseudo-CT	CAE	Brain	^{18}F-FDG
	Armanious [33]	NAC PET	Pseudo-CT	GAN	Brain	^{18}F-FDG
	Dong [31]	NAC PET	Pseudo-CT	CycleGAN	WB	^{18}F-FDG
NAC PET to Corrected PET	Shiri [29]	NAC PET	Corrected PET	CAE	Brain	^{18}F-FDG
	Dong [32]	NAC PET	Corrected PET	CycleGAN	WB	^{18}F-FDG
Improved Simultaneous Reconstruction	Hwang [26]	MLAA output	CT μ-map	CAE, U-net, Hybrid	Brain	^{18}F-FPCIT
	Hwang [28]	MLAA output	CT μ-map	U-net	WB	^{18}F-FDG
	Shi [25]	MLAA output	CT μ-map	U-net	WB	^{18}F-FDG

FCN: fully convolutional neural network, GAN: generative adversarial networks, CNN: convolutional neural network, CAE: convolutional auto-encoder, CED: convolutional encoder–decoder, UTE: ultra-short echo time, ZTE: zero echo time, NAC: non-attenuation-corrected, MLAA: maximum likelihood reconstruction of activity and attenuation

and structures for quantitative image analyses [201], [202], image spatial normalization [203], [204], voxel-based internal dosimetry [205], and the image-to-image transition for PET AC. Moreover, the DL-based lesion detection and image interpretation received significant research attention [206]–[209].

Several different DL-based approaches have been proposed for PET AC, as summarized in Fig. 17 and Table I. For the realization of improved AC in PET/MRI studies, deep neural networks are employed for the conversion of diagnostic or nondiagnostic MR images to a pseudo-CT or μ-map [34]–[44]. Alternative approaches are as follows: the derivation of pseudo-CT or attenuation-corrected PET images from NAC PET, and the improvement of the outputs of simultaneous activity and attenuation reconstruction using DL [25]–[33].

VIII. DEEP LEARNING: MRI TO CT

In recent years, significant research attention has been directed toward the derivation of pseudo-CT from MR images based on DL approaches. The objective of the above-mentioned studies was the utilization of MR images for PET AC in PET/MRI, and radiation treatment planning based on MRI [210]–[213]. In radiation treatment planning, the superior soft-tissue contrast of MRI relative to CT allows for a more accurate treatment target and normal structure delineation [214]. The MR-only simulation and planning based on the MRI-to-CT conversion has several advantages over those based on co-registered CT, namely, the minimization of the dosimetric error due to spatial misregistration and the temporal changes of anatomy between MRI and CT. Moreover, the inconveniences and costs of patients can be reduced by the elimination of redundant CT scans [215].

A. Diagnostic MRI to Pseudo-CT

The initial studies conducted on the utilization of DL methods for the generation of pseudo-CT from MRI were focused on the conversion of MR images obtained using routine diagnostic MR pulse sequences, such as $T1$ and $T2$ into the

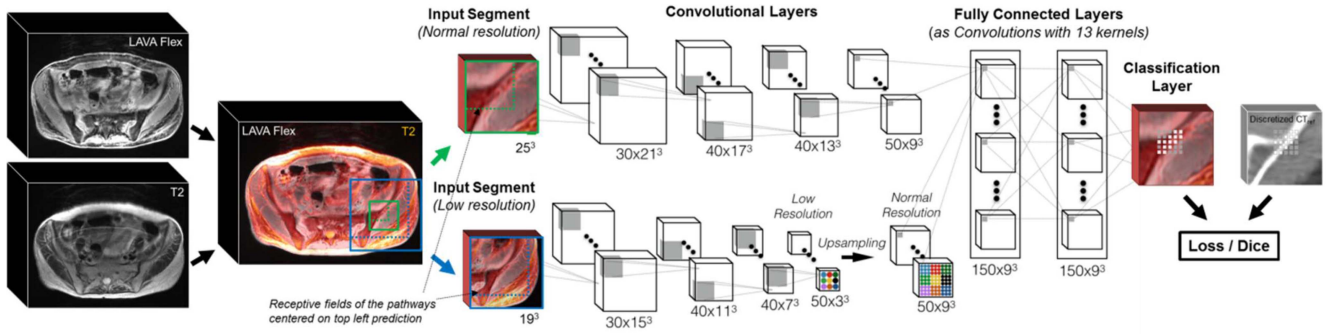

Fig. 18. Two parallel 3-D CNN pathways for multiscale patch-based learning of MRI-to-CT translation. (Reprint from [43] according to the publisher's open access policy.)

pseudo-CT images [38]–[44]. The $T1$-weighted MR images are obtained using a short TE and repetition time (TR), and their intensity contrast is predominately determined by the $T1$ relaxation properties of tissues. The $T1$ pulse sequence provides anatomical images with close proximity to the tissue appearances in the macro scale. The $T2$-weighted MRI is produced using long TE and TR times that yield the image contrast determined by the $T2$ relaxation properties. Unlike the UTE, ZTE, and Dixon MR images currently used for AC in PET/MRI, $T1$ and $T2$ images are obtained in almost all routine MRI protocols. Therefore, if the pseudo-CT or μ-map can be generated from the conventional $T1$- and/or $T2$-weighted MR images with sufficiently small PET quantification errors, the PET/MR imaging workflow can be considerably improved by eliminating the additional MR pulse sequences only required for PET AC with small diagnostic values.

In particular, Nie *et al.* employed a three-dimensional (3-D) fully convolutional neural network (FCN) that better preserves the neighborhood information in the predicted pseudo-CT than the conventional convolutional neural network (CNN), for the learning of end-to-end mappings from pelvic $T1$ MR images to their corresponding CT [40]. The mapping from an MRI patch with dimensions of $32 \times 32 \times 16$ to a CT patch with dimensions of $24 \times 24 \times 12$ was learned in this study using 6000 patches sampled from 21 pairs of CT and MRI volumes. Moreover, an adversarial training strategy was demonstrated for the training of the FCN, which allowed for a more accurate and robust synthesis of the pseudo-CT, and the loss function based on the image-gradient-difference alleviated the blurriness of the pseudo-CT [39]. Alternatively, the U-net architecture [216], which is widely used in medical image segmentation and other image-to-image translation tasks [202], [205], [217], was adopted for the conversion of a 2-D $T1$ MRI slice to its corresponding 2-D CT (2-D slice-to-slice mapping) [42]. In this study, the trained network using 2400 slices collected from 15 training subjects provided a significantly higher accuracy than the atlas-based method under evaluation using three different metrics computed between the original and synthetic head CTs (voxel-wise mean absolute error, mean-squared error, and Pearson correlation in pixel intensity). Bradshaw *et al.* [43] used $T2$ and $T1$ LAVA Flex MR images as inputs to a deep network that generates a four-class μ-map for pelvic PET/MRI studies. The network used

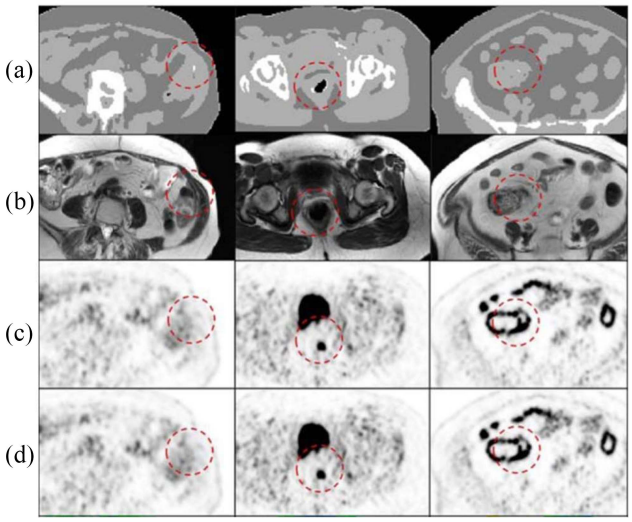

Fig. 19. Negligible impact of small errors in the pseudo-CT generation on the corrected PET images: (a) pseudo-CT generated using CNNs, (b) corresponding $T2$ MRI, (c) corrected PET images using pseudo-CT, and (d) corrected PET images using ground-truth CT. (Reprint from [43] according to the publisher's open access policy.)

in this study has two 3-D CNN pathways for the patch-based learning of MRI-to-CT translation. The two parallel CNN pathways trained simultaneously and then combined via fully connected layers handled different receptive fields relative to the input image, thus allowing for multiscale processing. This is necessary for the efficient utilization of local and contextual information, which is useful for a better understanding of the complex anatomy of the human body (Fig. 18) [218]. Although several errors were observed in the four-class μ-map generated by the network, e.g., discontinuous bone segments and misplaced bone, they were found to have a negligible impact on the corrected PET images (Fig. 19).

Unlike CT, the same MRI pulse sequence can yield different image intensities and contrasts depending on the magnet field strength and scanner type [42]. Liu *et al.* [41] addressed this major technical issue in DL-based MRI-to-CT translation. In this study, a convolutional autoencoder (CAE) network that learned MRI-to-CT mapping based on $T1$-weighted MR images obtained using a 1.5-T MR scanner was applied to data obtained at 3.0-T MR scanner with a $T1$ pulse sequence. It should be noted that the CAE that learned the translation

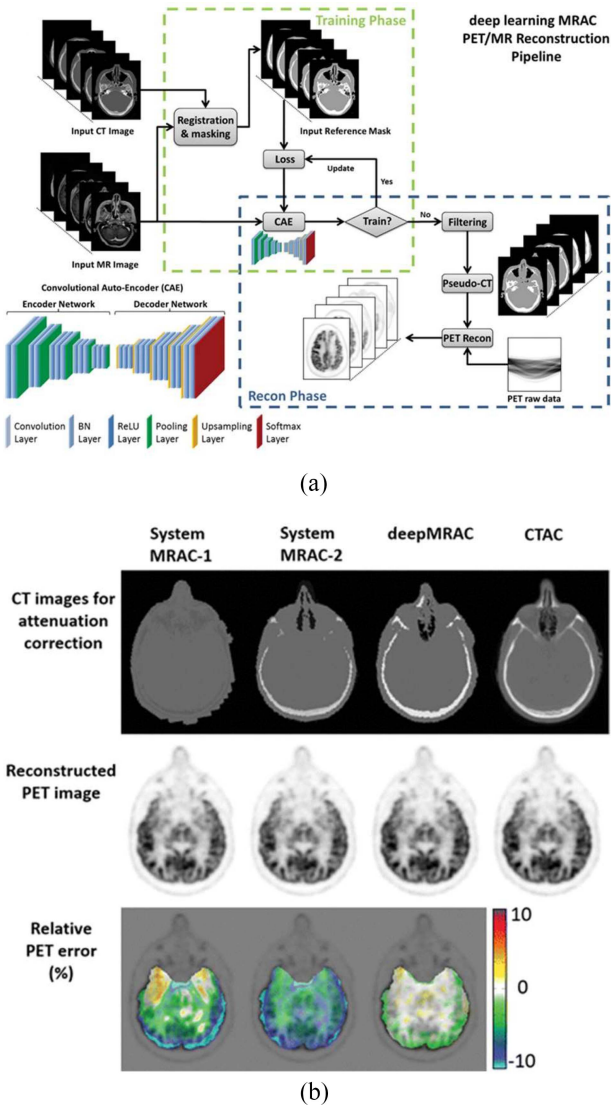

Fig. 20. Feasibility study of applying MRI-to-CT translation rule learned from 1.5-T MR images to 3.0-T. (a) Pipeline for pseudo-CT generation and PET reconstruction. (b) Superior performance of DL-based AC (deepMRAC) to Dixon MRI-based (System MRAC-1) and atlas-based (System MRAC-2) AC. (Reprint from [41] with permission; © 2018 RSNA.)

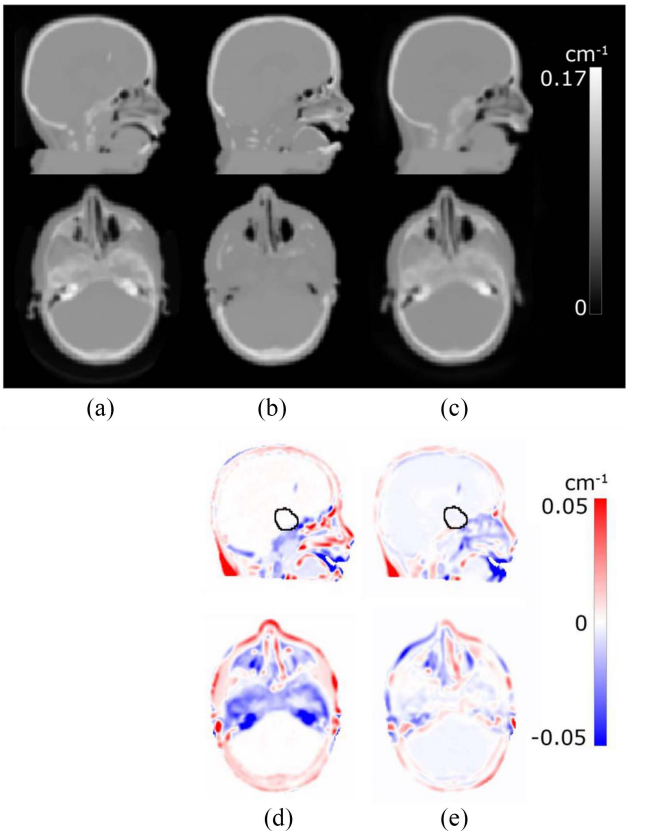

Fig. 21. DL-based pseudo-CT generation from UTE MRI: (a) ground-truth CT, (b) UTE only, (c) UTE and DL, (d) subtraction of (a) from (b), and (e) subtraction of (a) from (c). (Reprint from [36] according to the publisher's open access policy.)

rule from the 1.5-T MR exhibited a remarkable performance for 3.0-T images. In addition, the CAE network yielded more accurate results to other conventional MR-based AC methods in brain ^{18}F-FDG PET/MRI studies (Dixon- and atlas-based) with respect to the similarity of the μ-map with CT-based map, and the accuracy of the attenuation-corrected PET activity (Fig. 20).

B. Nondiagnostic MRI to Pseudo-CT

It has been demonstrated that DL approaches are useful for the improvement of the generation of μ-maps from UTE, ZTE, and Dixon MRIs currently used in clinical PET/MRI systems for AC [34]–[37]. Moreover, the DL is an effective method for the integration of multiparametric information provided by different MR sequences, for the generation of more accurate μ-maps. The use of PET/MRI specific MR pulse sequences as input data to the deep neural network would be more effective than the use of conventional $T1$- and $T2$-weighted MRI inputs for μ-map generation, given that they were designed to allow for better bone delineation or water/fat segmentation. Jang *et al.* [37] trained a convolutional encoder–decoder (CED) network that was pretrained with $T1$-weighted MR images to yield air, soft tissue, and bone labels from UTE image inputs. For the generation of pseudo-CT images, the tissue labels estimated by the CED network were refined by the application of a conditional random field-based correction [219], and then combined with fat and water images generated using a dual-echo ramped hybrid encoding (dRHE) pulse sequence that allows for UTE, fat, and water images to be obtained with a short scan time (35 s). In brain PET/MRI studies using ^{18}F-FDG, the DL-based approach outperformed the vendor's soft-tissue-only and the atlas-based ACs, in addition to the previous approach with dRHE acquisition and histogram-based image segmentation. Alternatively, a U-net-based network was trained by Ladefoged *et al.* to yield pseudo-CT from UTE images [36]. In this approach, 16 neighboring slices were employed for each of the two echo images obtained using echo times of 0.07 and 2.46 ms, and the R_2*-map derived from the echo images were used as inputs to the 3-D U-net. In the O-(2-^{18}F-fluoroethyl)-L-tyrosine (^{18}F-FET) brain PET/MRI studies, the DL-based method allowed for a more robust AC than the RESOLUTE method, which was previously proposed (Fig. 21) [124].

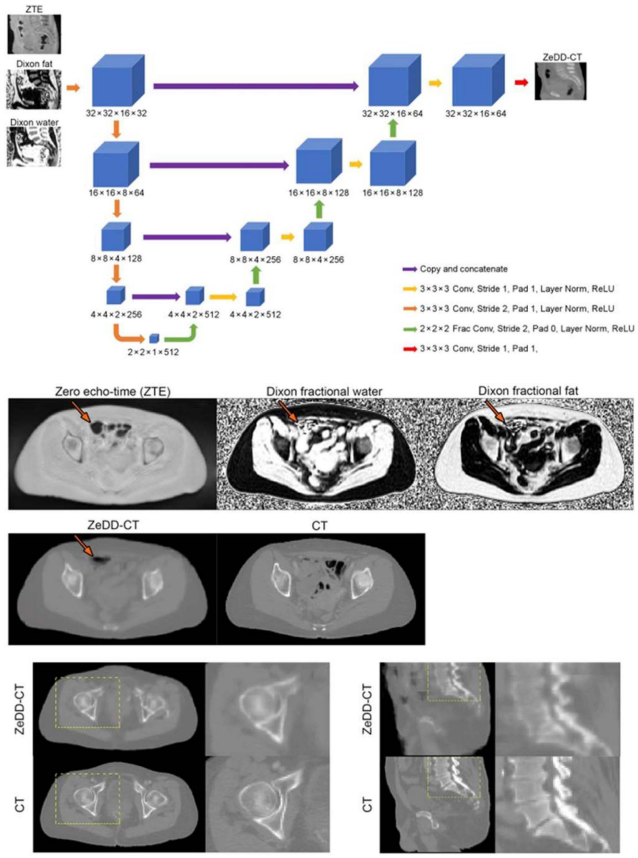

Fig. 22. DL-based integration of multiparametric MR information to obtain pseudo-CT (ZeDD-CT) for pelvic PET/MRI: network structure and comparison with ground-truth CT. (Reprint from [35] with permission; © 2018 SNMMI.)

The DL-based approaches improved the AC in pelvic PET/MRI studies. Leynes *et al.* [35] demonstrated the high efficiency of DL-based information integration provided by multiparametric MR pulse sequences for PET AC in pelvic PET/MRI. The patch-based learning of a CNN based on the *U*-net architecture was conducted using a bias-corrected and soft-tissue-normalized proton-density ZTE image, Dixon fractional fat image, and Dixon fractional water image as inputs. Fig. 22 presents the output images (ZeDD-CT) from the deep neural network, which can depict bone structures and soft tissues without the application of segmentation or other image processing, with the exception for the bias correction and soft-tissue normalization in ZTE images. For the evaluation of the trained network on 30 bone lesions and 60 soft-tissue lesions in pelvic ^{18}F-FDG and ^{68}Ga-PSMA-11 PET/MRI studies, the error in PET quantification was reduced by a factor of 4 in bone lesions and by a factor of 1.5 in soft-tissue lesions (the root-mean-squared error by DL was 2.68% and 4.07% in bone and soft tissue, respectively). Moreover, Torrado-Carvajal *et al.* [34] investigated the feasibility of only using the Dixon images as inputs to the deep neural network for AC in pelvic PET/MRI. In this study, four 2-D slices (water, fat, in-phase, and out-of-phase) of Dixon-VIBE MR images were provided to a CNN as inputs, to yield corresponding pseudo-CT slices (Fig. 23). The DL approach resulted in a decrease in the PET quantification error in bone

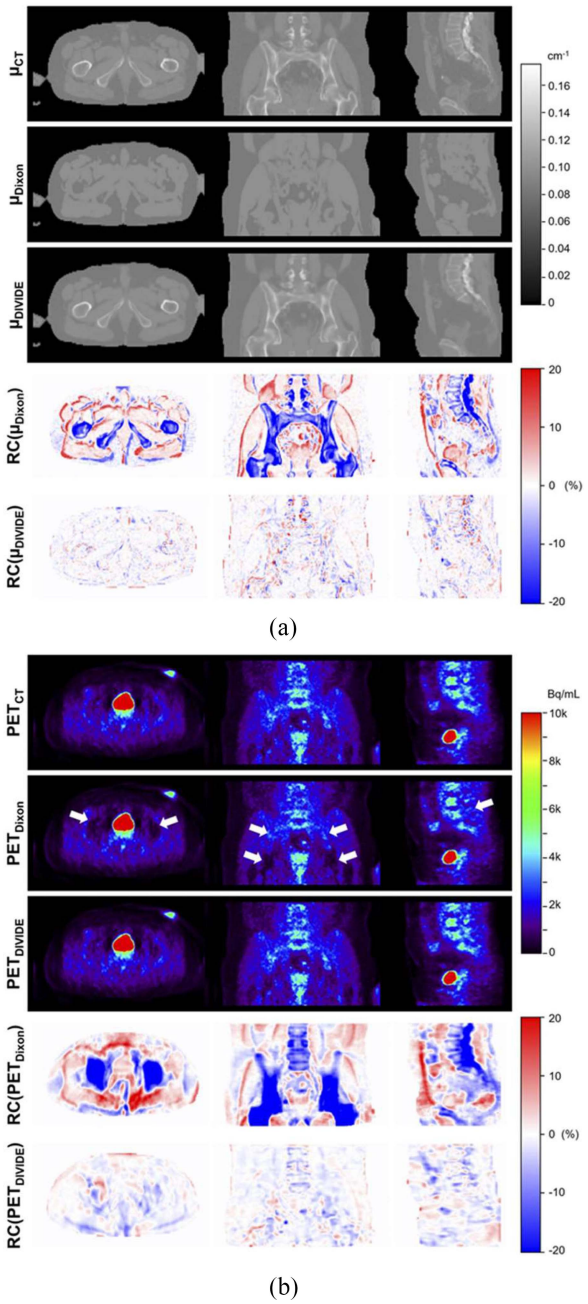

Fig. 23. DL-based pseudo-CT generation from Dixon MRI (DIVIDE: Dixon-ViBE deep learning): (a) μ-maps and (b) PET images. (Reprint from [34] with permission; © 2019 SNMMI.)

tissue by a factor of 6.75, relative to conventional Dixon-based AC. The variability in the error was reduced by a factor 3.5, which indicates that the DL-based method yields a more precise PET quantification. This approach has the advantages of a shorter MR scan time than that obtained with the ZTE and Dixon combination as inputs, given that only the standard Dixon-VIBE images are used, thus allowing for the retrospective processing of already obtained PET/MRI data with only Dixon-VIBE sequence for AC.

IX. Deep Learning: Emission-Only Approaches

The PET AC based only on the emission PET data and deep neural network with no anatomical image input is more

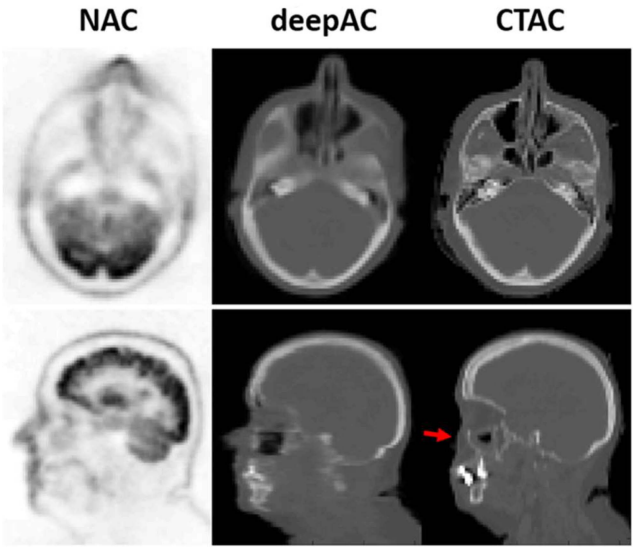

Fig. 24. Robustness of DL-based emission-only pseudo-CT generation to head movement between CT and PET scans. The red arrow indicates a noticeable movement. (Reprint from [30] according to the publisher's open access policy.)

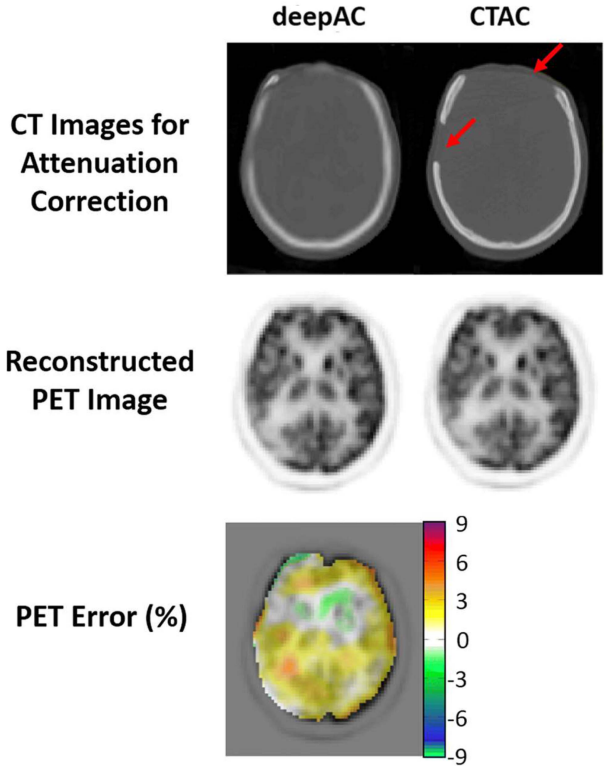

Fig. 25. Prediction of missing parts in the skull by DL-based pseudo-CT generation from NAC PET. (Reprint from [30] according to the publisher's open access policy.)

challenging than previously described anatomical image-based approaches. However, the methods that are only dependent on the emission PET have several advantages over the anatomical image-based approaches. When the neural networks are trained for AC, these approaches are not subject to the errors due to the different positioning and organ displacement during the scan. Moreover, they can be applied to PET/CT and stand-alone PET data in addition to PET/MRI.

A. NAC PET to Pseudo-CT

One of these emission-only approaches is utilizing NAC PET images as input to generate pseudo-CT [30], [31], [33] or attenuation-corrected PET images [29], [32]. Liu *et al.* [30] trained a CAE modified to have a *U*-net-like structure through the addition of symmetrical short connections between encoding and decoding stages to generate pseudo-CT images from NAC PET by using 100 ^{18}F-FDG brain PET/CT datasets. The average absolute ROI-level error in the reconstructed PET images of the 28 testing subjects was less than 3% in the 21 brain regions evaluated. The error in pseudo-CT generation due to head movement between PET and CT scans was also mitigated by applying this emission-only approach (Fig. 24). In addition, the missing parts of the skull could be predicted by the network in pseudo-CT, although no anatomical information was provided to the network (Fig. 25). Armanious *et al.* [33] also demonstrated the feasibility of generating pseudo-CT from NAC ^{18}F-FDG brain PET images for which they used generative adversarial networks (GANs) trained with 50 PET/CT datasets. To translate 2-D NAC PET slices into corresponding pseudo-CT slices, they utilized the conditional GAN framework. In this framework, a generator network converts NAC PET into pseudo-CT, and a discriminator network distinguishes the pseudo-CT from the corresponding ground-truth CT. Both these networks were simultaneously trained. No differences in diagnostic image information were observed between PET images corrected for attenuation using ground truth and pseudo-CT when the clinical evaluation was conducted on 20 datasets of various brain disorders. The absolute SUV error over all the brain regions was less than 5%. To generate pseudo-CT from NAC PET for whole-body PET studies, Dong *et al.* [31] utilized a cycle-consistent GAN (CycleGAN) framework (Fig. 26). This method simultaneously learned targeted transformation from NAC PET to pseudo-CT and its inverse transformation using 3-D patches extracted from 80 whole-body oncologic ^{18}F-FDG PET/CT studies. In the CycleGAN framework, a self-attention *U*-net architecture, in which attention gates are integrated into a standard *U*-net architecture for better identification of semantic contextual information and mitigation of noise disturbance, was used as a generator. In addition, a fully convolutional network was used as a discriminator in the CycleGAN framework. A validation study on 39 independent patients showed that the mean absolute error between pseudo-CT and ground-truth CT was less than 110 HU. The mean error and normalized mean-squared error in the PET quantification of the brain, heart, left kidney, right kidney liver, and lesion ranged from -1.06% to 3.57% and 0.43% to 1.80%, respectively. However, the errors were large in the lung, mainly owing to tissue heterogeneity, and no evaluation results on bone lesions were reported.

B. NAC PET to Corrected PET

The generation of attenuation-corrected PET images directly from NAC PET images can prevent errors due to misalignment and misregistration between different modality images

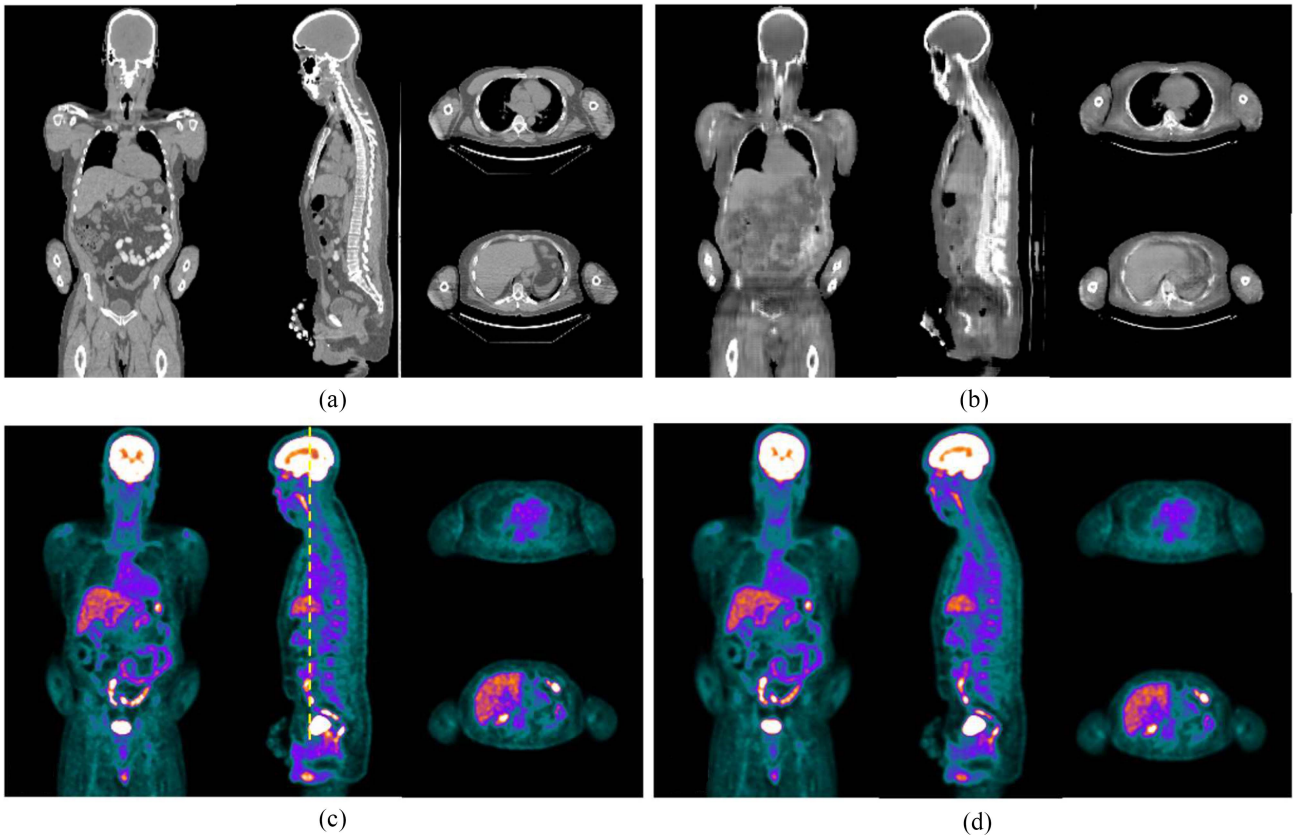

Fig. 26. DL-based pseudo-CT generation from NAC whole-body PET images. (a) Ground-truth CT. (b) Pseudo-CT from NAC PET. (c) Corrected PET using ground-truth CT. (d) Corrected PET using pseudo-CT. (Reprint from [31] with permission; © 2019 IPEM.)

while training and testing the networks. The processing time is also shorter for PET AC because additional image reconstruction is not necessary. A deep CAE was utilized by Shiri *et al.* for the direct transition of ^{18}F-FDG brain PET images [29]. Their results demonstrated a high peak signal-to-noise ratio (39.2±3.65) and structural similarity index metric (0.989±0.006) between the predicted and ground-truth attenuation-corrected PET images, leading to the low mean relative error in SUV_{mean} (0.02%) and SUV_{max} (−3.87%) quantification. The same approach was also used for the AC in whole-body ^{18}F-FDG PET images by Dong *et al.* (Fig. 27) [32]. This study was conducted using a 3-D patch-based CycleGAN framework, and the average mean error and normalized mean-square error between attenuation-corrected PET images by using the CycleGAN framework and CT-based AC were 0.62% and 0.72% for whole-body PET. The performance of the CycleGAN framework was better than that of the *U*-net architecture and GAN. Although this direct conversion approach was feasible in these initial studies, it should be noted that the DL error in this approach directly leads to PET quantification error in the image space.

C. Improved Simultaneous Reconstruction

Another emission-only approach is improving the accuracy of simultaneously reconstructed activity and μ-maps by using DL [25]–[28], [220], [221]. As previously mentioned, joint emission and transmission estimation algorithms augmented by accurate TOF information allow the simultaneous reconstruction of activity image and μ-map (or ACF) [173]–[180]. The μ-map generated by applying the MLAA algorithm to uncorrected emission PET data is directly related to the attenuation coefficient of tissues for 511-keV annihilation photons. In addition, the MLACF provides an ACF that contains fundamentally the same information. However, the quality and accuracy of these joint estimation algorithms are not sufficiently good for clinical routine use mainly because of the limited timing resolution of current PET scanners. In addition, the simultaneous reconstruction algorithms require a refined calibration of the TOF PET system and improved modeling of the PET acquisition physics [222].

To overcome the limitations of current simultaneous reconstruction algorithms, Hwang *et al.* [26] proposed a DL-based enhancing method and verified its feasibility by using clinical brain PET/CT datasets. In this initial study, three different CNN architectures (CAE, *U*-net, and hybrid of CAE and *U*-net) were designed and trained using 2-D slices of MLAA activity image and μ-map to learn CT-based μ-map (Fig. 28). To demonstrate the feasibility of the proposed method, the authors chose ^{18}F-fluorinated-N-3-fluoropropyl-2-β-carboxymethoxy-3-β-(4-iodophenyl)nortropane (^{18}F-FP-CIT) brain PET/CT dataset, one of the most challenging datasets for simultaneous reconstruction due to severe crosstalk between activity and attenuation and the high background noise in the

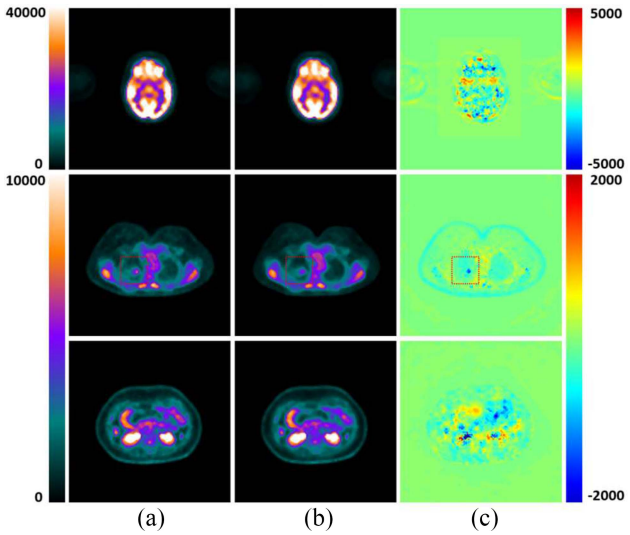

Fig. 27. DL-based direct generation of attenuation-corrected PET images from NAC PET. (a) CT AC. (b) DL-based approach. (c) Difference. (Reprint from [32] with permission; © 2020 IPEM.)

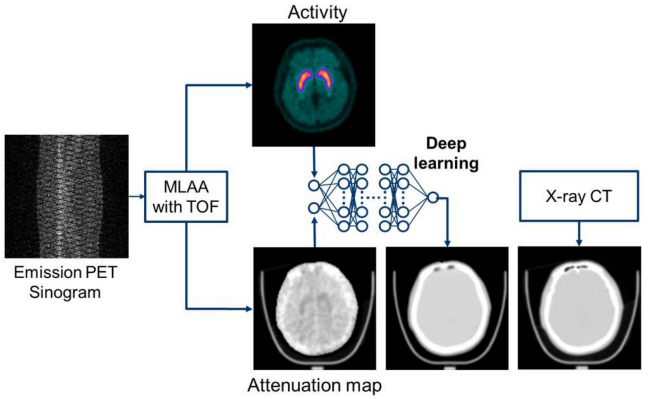

Fig. 28. Improving the accuracy of simultaneously reconstructed activity and attenuation maps using DL. (Reprint from [26] with permission; © 2018 SNMMI.)

nonspecific binding brain regions. The networks were trained with 800 000 slices that were obtained by applying augmentation methods (rotation and flipping) to 32 patients' datasets. These networks remarkably reduced the noise and crosstalk in the MLAA-generated μ-maps. Among the three network architectures, the hybrid network of CAE and *U*-net yielded the most similar μ-maps to CT-based μ-maps: the Dice similarity coefficient between CT-based and DL-based μ-maps in the whole head was 0.79 in the bone and 0.72 in air cavities. The error in the regional activity and binding ratio quantification was only approximately 5% when the hybrid network was applied.

This DL approach, which enhanced the accuracy of simultaneously reconstructed μ-map, was further improved by applying 3-D patch-based learning. Choi *et al.* [220] compared the performance of 2-D slice-to-slice and 3-D patch-to-patch transition strategies to improve the MLAA μ-map. In this study, four different *U*-net models (2-D, 2-D residual, 3-D, and 3-D residual *U*-nets) were trained and tested with ^{18}F-florbetaben brain PET/CT scan data of 78 subjects suspected with Alzheimer's disease. The results showed that 3-D patch-based learning was superior to 2-D slice-based learning: Dice similarity coefficient with CT-based μ-maps for bone in the head region was 0.67 and 0.80 in the 2-D *U*-net and 3-D *U*-net, respectively. In addition, the 3-D patch-based learning allowed better continuity of μ-map in the axial direction. The residual learning was only useful for 2-D slice-based learning. The 3-D patch-based learning with *U*-net has also improved the MLAA μ-map and PET quantification in the whole-body ^{18}F-FDG PET studies (Fig. 29) [28]. In his study, which was conducted with PET/CT dataset of 100 patients, a 3-D *U*-net trained with 1.3 million patches derived from 60 whole-body PET/CT dataset improved the Dice similarity in bone tissues from 0.36 (original MLAA) to 0.77 (DL-enhanced MLAA); moreover, the standard uptake value (SUV) correlation (R^2) in suspicious bone lesions improved from 0.91 (original MLAA) to 0.99 (DL-enhanced MLAA). The authors also showed the strong potential of improved AC by this method in whole-body PET/MRI studies: relative to the four-segment map derived from CT, the deep-leaning-enhanced MLAA showed considerably higher peak signal-to-noise ratio in attenuation-corrected activity map (60.4 versus 49.9) and lower SUV quantification error in vertebral lesions (-2.2% versus -9.4%).

Another approach to improve the DL-enhanced MLAA is applying acquisition physics-based additional constraints in the projection domain of the μ-map. Shi *et al.* [25] enforced the similarity in the projection domain between the predicted and CT-based μ-maps based on the fact that the line integral of the attenuation coefficient along the LOR is used for AC instead of attenuation coefficient itself. By adding the loss function that measures the line-integral difference between predicted and CT-based patches (projection domain) to the loss function that measures image intensity and gradient differences (image domain), more accurate μ-maps and corrected PET images could be obtained. This study is a good example demonstrating how a better understanding of PET acquisition physics and correction algorithms can result in better DL performance for PET AC.

The advantages of emission-only approaches were better demonstrated by the deep-leaning-enhanced MLAA. Because attenuation coefficients are estimated from the uncorrected emission PET data acquired with monoenergetic 511-keV annihilation photons, metal artifacts caused by the low-energy photon starving in X-ray CT were not observed in simultaneously estimated μ-maps (Fig. 30); this enables more accurate PET AC in patients with metallic implants [27]. In addition, there is no time discrepancy between the activity and attenuation information that is derived only from the emission measurement; this allows for better spatiotemporal correlation between activity images and μ-maps as well as lower error associated with their spatiotemporal mismatch. Fig. 31 shows how DL-enhanced MLAA mitigates the arm position mismatch artifact that is frequently observed in PET and CT scans [25]. In addition, the difference between the CT-based and DL-enhanced MLAA-based attenuation-corrected whole-body PET images was the largest in lung boundary and upper liver dome, which are most vulnerable to the position mismatch artifacts caused by respiratory motion in PET/CT

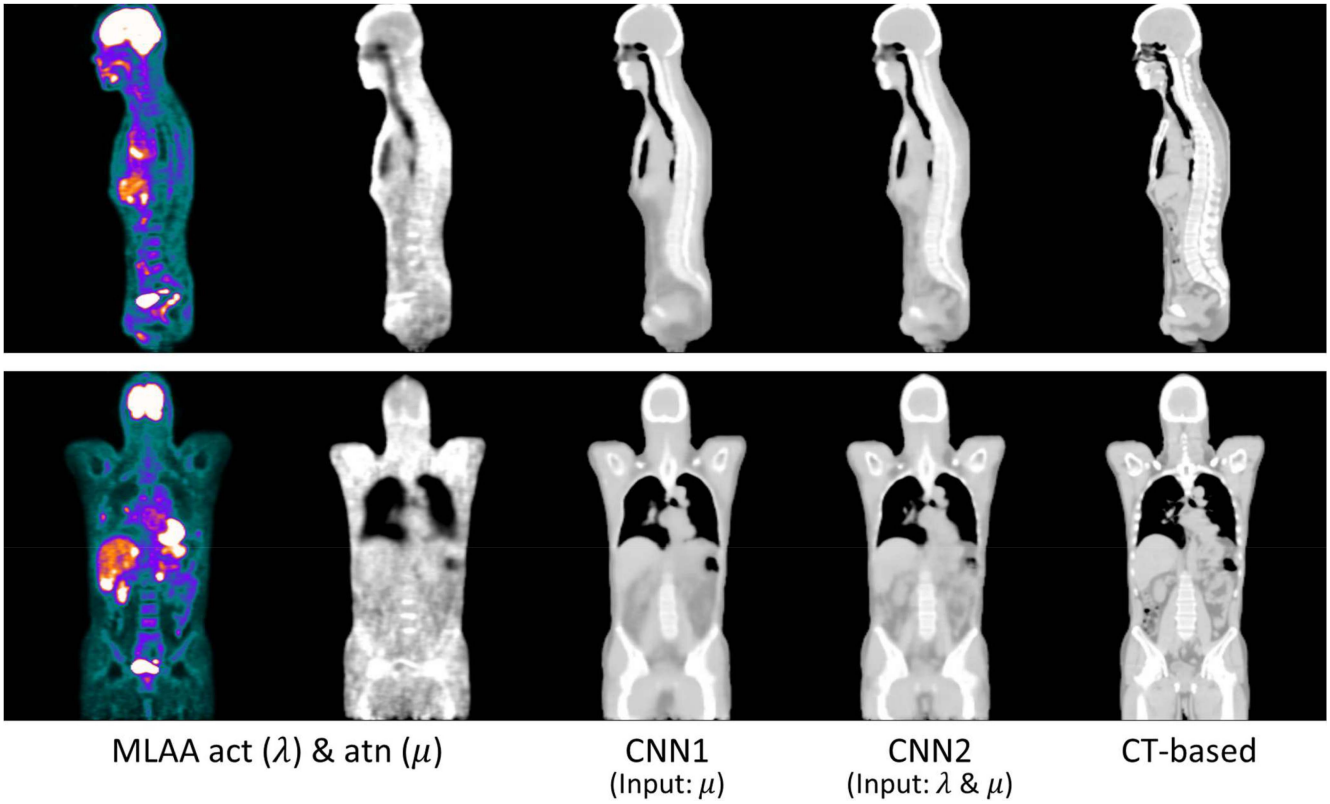

Fig. 29. Improved MLAA μ-maps by DL in whole-body ^{18}F-FDG PET studies. (Reprinted from [28] with permission; © 2019 SNMMI.)

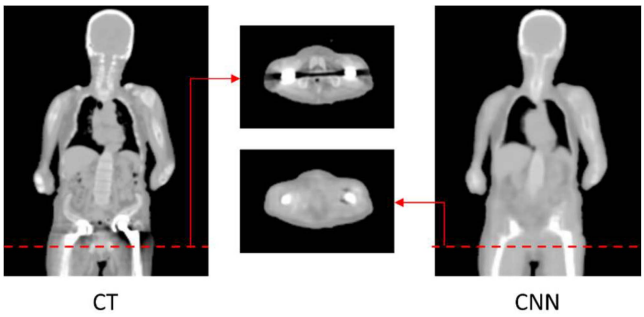

Fig. 30. Absence of metal artifacts in the μ-map derived from emission data using MLAA and DL.

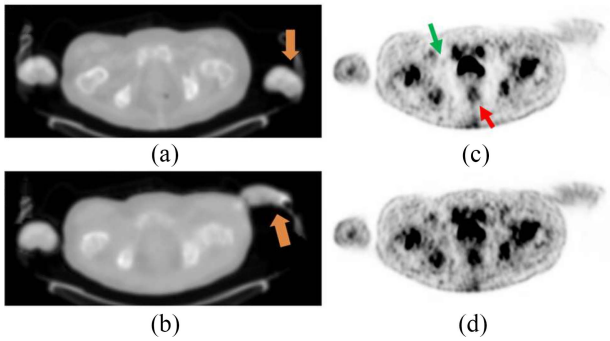

Fig. 31. Mitigation of arm position mismatch artifact using MLAA and DL: (a) CT-based μ-map, (b) μ-map derived from emission data using MLAA and DL, (c) corrected PET using CT-based μ-map, and (d) corrected PET using MLAA and DL. (Courtesy of Yihuan Lu at Yale University.)

studies [28]. This observation indicates the reduction of the mismatch artifacts by the MLAA and DL. This approach also allowed a further improvement in the position-mismatch artifact reduction by enabling the respiratory phase-matched AC in PET/CT [221]. In this study, MLAA reconstruction was applied to every respiratory-gated emission PET frame that was generated using a data-driven gating method, and the gated μ-maps were enhanced by the DL and used for deriving motion vector fields between the gating phases; these vector fields were used to generate motion-free phase-matched attenuation-corrected PET images.

X. Deep Learning: Future Direction

Previous studies reviewed in this article have shown that DL is a useful approach to improve the accuracy of AC in PET/MRI. Moreover, the DL-based approaches that do not require MRI input can be utilized for various types of artifact reduction in AC for PET/CT. However, such promising results were mostly obtained from the regional ^{18}F-FDG PET scans on the brain and pelvic region, where the large-sized bone structures with relatively simple shapes, such as skull, hip bones, and femur, are dominant attenuating materials. In addition, photon-counting statistics in the regional PET scans are better than multibed whole-body scans. Therefore, further investigations are required to prove the feasibility of proposed approaches in the application to whole-body PET studies with lower counting statistics and radiotracers other than ^{18}F-FDG.

A major obstacle in whole-body PET/MRI AC investigations is the limited availability of a large number of registered

TABLE II
PROS AND CONS OF DL-BASED APPROACHES FOR PET AC

Approach	Pros	Cons
Diagnostic MRI to Pseudo-CT	- No additional MR pulse sequences for AC	- Subject to MRI artifacts and PET/MRI misalignment error - Worse physical relevance
Non-diagnostic MRI to Pseudo-CT	- Better physical relevance - Better bone delineation and water/fat separation	- Subject to MRI artifacts and PET/MRI misalignment error - Additional MR pulse sequences for AC - PET/MRI only
NAC PET to Pseudo CT	- No anatomical images and misalignment error - Stand-alone PET applicability - Easy implementation	- Limited bone and air cavity delineation - Large error in lung
NAC PET to Corrected PET	- No anatomical images and misalignment error - Stand-alone PET applicability - Easy implementation and shorter processing time	- Limited bone and air cavity delineation - Non-availability of μ-maps - Direct influence of DL error on PET quantification
Improved Simultaneous Reconstruction	- No anatomical images and misalignment error - Stand-alone PET applicability - Better physical relevance	- Additional image reconstruction - Necessity of time-of-flight information - Low resolution of μ-maps

TABLE III
PROS AND CONS OF DEEP NEURAL NETWORK MODELS USED FOR PET AC

Learning model	Pros	Cons
Discriminative (e.g., CAE, CED, and U-net)	- Simple and stable - Easy to train	- Blurry output image - Weaker generalization power
Generative (e.g., GAN)	- More realistic output image - Possible semi-supervised learning	- Complex and unstable - Hallucination artifact

CAE: convolutional auto-encoder, CED: convolutional encoder–decoder, GAN: generative adversarial networks

CT and MRI pairs and the lack of accuracy of nonlinear registration between them. A promising approach to overcome this challenge is the use of CycleGAN that employs cycle consistency loss as an indirect structural similarity between the input and synthesized images [223]–[225]. Further evaluation of this method for PET/MRI AC will be necessary.

The pros and cons of different DL-based AC methods and neural network models used for them are summarized in Tables II and III. However, it is currently difficult to identify the approaches and algorithms that can be employed for the best performance of the DL-based AC method for PET/CT and PET/MRI because each group uses different performance matrices, and there is no available standard reference dataset and processing pipeline to compare the performance of each method. The research community should consider the establishment of a standard dataset and evaluation framework for this important but challenging task in nuclear medicine [20]. In addition, the investigators should further consider identifying the best input to the deep neural networks, to derive the most accurate and robust attenuation-corrected PET images. In this respect, a synergistic combination of different approaches to achieve the best outcome should be considered. Most of the previous investigations have used only a single type of dataset as an input to the deep neural networks. However, using multiscale, multisequence, and multiparametric inputs to the networks seems to be a useful approach to enhance the performance of DL-based AC methods [26], [28], [35], [43]. Moreover, an overlooked aspect, which has not been considered as an input to the networks, is the distribution of scattered photons that is closely related with μ-map. Given that the attenuation in PET is mainly due to Compton scattering and several studies are showing the usefulness of the

scattered coincidence measurements for improving the PET AC [226]–[229], the DL-based scatter-to-attenuation approach looks promising.

AC is also important for SPECT because of the increasing use of theranostic agents that emit single gamma-ray photons [5], [230]–[232]. Accurate absorbed radiation dose estimation at voxel and organ level is only possible with quantitively accurate SPECT data that is corrected for attenuation, scatter, and collimator-detector response. In addition, the use of quantitative SPECT for diagnostic purposes is increasing [233]. However, the SPECT/CT that allows accurate SPECT quantification is not widely available yet. A few emission-only approaches used for DL-based PET AC will be potentially useful for SPECT AC. Further development of a unique approach to SPECT AC will be also necessary.

ACKNOWLEDGMENT

The author would like to thank Donghwi Hwang, Seung Kwan Kang, and Seok Hwan Yoon for their assistance with manuscript preparation and Tyler Bradshaw at University of Wisconsin–Madison and Yihuan Yu at Yale University for providing figures.

REFERENCES

[1] J. S. Lee, "Basic nuclear physics and instrumentation," in *Handbook of Nuclear Medicine and Molecular Imaging: Principles and Clinical Applications*, E. Kim, D. Lee, U. Tateishi, and R. Baum, Eds. Singapore: World Sci., 2012, pp. 3–19.

[2] D. L. Bailey, "Transmission scanning in emission tomography," *Eur. J. Nucl. Med.*, vol. 25, no. 7, pp. 774–787, 1998.

[3] H. Zaidi and B. Hasegawa, "Determination of the attenuation map in emission tomography," *J. Nucl. Med.*, vol. 44, no. 2, pp. 291–315, 2003.

[4] Y. Y. Choi, J. S. Lee, and S.-O. Yang, "Musculoskeletal lesions: Nuclear medicine imaging pitfalls," in *Pitfalls in Musculoskeletal Radiology*, W. C. G. Peh, Ed. Cham, Switzerland: Springer, 2017, pp. 951–976.

[5] J. S. Lee and J. H. Kim, "Recent advances in hybrid molecular imaging systems," *Seminars Musculoskeletal Radiol.*, vol. 18, no. 2, pp. 103–122, 2014.

[6] Y. Seo, C. Mari, and B. H. Hasegawa, "Technological development and advances in single-photon emission computed tomography/computed tomography," *Seminars Nucl. Med.*, vol. 38, no. 3, pp. 177–198, 2008.

[7] D. W. Townsend, "Dual-modality imaging: Combining anatomy and function," *J. Nucl. Med.*, vol. 49, no. 6, pp. 938–955, 2008.

[8] C. Burger, G. Goerres, S. Schoenes, A. Buck, A. H. Lonn, and G. K. Von Schulthess, "PET attenuation coefficients from CT images: Experimental evaluation of the transformation of CT into PET 511-keV attenuation coefficients," *Eur. J. Nucl. Med. Mol. Imag.*, vol. 29, no. 7, pp. 922–927, 2002.

[9] P. E. Kinahan, B. H. Hasegawa, and T. Beyer, "X-ray-based attenuation correction for positron emission tomography/computed tomography scanners," *Seminars Nucl. Med.*, vol. 33, no. 3, pp. 166–179, 2003.

[10] P. E. Kinahan, D. W. Townsend, T. Beyer, and D. Sashin, "Attenuation correction for a combined 3D PET/CT scanner," *Med. Phys.*, vol. 25, no. 10, pp. 2046–2053, 1998.

[11] J. F. Barrett and N. Keat, "Artifacts in CT: Recognition and avoidance," *Radiographics*, vol. 24, no. 6, pp. 1679–1691, 2004.

[12] T. Beyer, G. Antoch, T. Blodgett, L. F. Freudenberg, T. Akhurst, and S. Mueller, "Dual-modality PET/CT imaging: the effect of respiratory motion on combined image quality in clinical oncology," *Eur. J. Nucl. Med. Mol. Imag.*, vol. 30, no. 4, pp. 588–596, 2003.

[13] G. W. Goerres, S. I. Ziegler, C. Burger, T. Berthold, G. K. Von Schulthess, and A. Buck, "Artifacts at PET and PET/CT caused by metallic hip prosthetic material," *Radiology*, vol. 226, no. 2, pp. 577–584, 2003.

[14] E. M. Kamel, C. Burger, A. Buck, G. K. von Schulthess, and G. W. Goerres, "Impact of metallic dental implants on CT-based attenuation correction in a combined PET/CT scanner," *Eur. Radiol.*, vol. 13, no. 4, pp. 724–728, 2003.

[15] M. M. Osman, C. Cohade, Y. Nakamoto, and R. L. Wahl, "Respiratory motion artifacts on PET emission images obtained using CT attenuation correction on PET-CT," *Eur. J. Nucl. Med. Mol. Imag.*, vol. 30, no. 4, pp. 603–606, 2003.

[16] Y. Chen and H. An, "Attenuation correction of PET/MR imaging," *Mag. Resonance Imag. Clin. North America*, vol. 25, no. 2, pp. 245–255, 2017.

[17] A. Mehranian, H. Arabi, and H. Zaidi, "Magnetic resonance imaging-guided attenuation correction in PET/MRI: Challenges, solutions, and opportunities," *Med. Phys.*, vol. 43, no. 3, pp. 1130–1155, 2016.

[18] S. Vandenberghe and P. K. Marsden, "PET-MRI: a review of challenges and solutions in the development of integrated multimodality imaging," *Phys. Med. Biol.*, vol. 60, no. 4, pp. pp. R115–R154, 2015.

[19] H. J. Yoo, J. S. Lee, and J. M. Lee, "Integrated whole body MR/PET: Where are we?" *Korean J. Radiol.*, vol. 16, no. 1, pp. 32–49, 2015.

[20] C. N. Ladefoged *et al.*, "A multi-centre evaluation of eleven clinically feasible brain PET/MRI attenuation correction techniques using a large cohort of patients," *Neuroimage*, vol. 147, pp. 346–359, Feb. 2017.

[21] A. J. González, F. Sánchez, and J. M. Benlloch, "Organ-dedicated molecular imaging systems," *IEEE Trans. Radiat. Plasma Med. Sci.*, vol. 2, no. 5, pp. 388–403, Sep. 2018.

[22] J. S. Lee, "Technical advances in current PET and hybrid imaging systems," *Open Nucl. Med. J.*, vol. 2, pp. 192–208, Dec. 2010.

[23] R. D. Badawi *et al.*, "First human imaging studies with the EXPLORER total-body PET scanner," *J. Nucl. Med.*, vol. 60, no. 3, pp. 299–303, 2019.

[24] S. Surti, A. R. Pantel, and J. S. Karp, "Total body PET: Why, how, what for," *IEEE Trans. Radiat. Plasma Med. Sci.*, vol. 4, no. 3, pp. 283–292, May 2020.

[25] L. Shi *et al.*, "A novel loss function incorporating imaging acquisition physics for PET attenuation map generation using deep learning," in *Proc. Med. Image Comput. Comput. Assist. Intervention*, 2019, pp. 723–731.

[26] D. Hwang *et al.*, "Improving the accuracy of simultaneously reconstructed activity and attenuation maps using deep learning," *J. Nucl. Med.*, vol. 59, no. 10, pp. 1624–1629, 2018.

[27] D. Hwang *et al.*, "Accurate attenuation correction for whole-body Ga-68-DOTATOC PET studies using deep learning," *J. Nucl. Med.*, vol. 60, no. S1, p. 568, 2019.

[28] D. Hwang *et al.*, "Generation of PET attenuation map for whole-body time-of-flight 18F-FDG PET/MRI using a deep neural network trained with simultaneously reconstructed activity and attenuation maps," *J. Nucl. Med.*, vol. 60, no. 8, pp. 1183–1189, 2019.

[29] I. Shiri *et al.*, "Direct attenuation correction of brain PET images using only emission data via a deep convolutional encoder–decoder (Deep-DAC)," *Eur. Radiol.*, vol. 29, no. 12, pp. 6867–6879, 2019.

[30] F. Liu, H. Jang, R. Kijowski, G. Zhao, T. Bradshaw, and A. B. McMillan, "A deep learning approach for ^{18}F-FDG PET attenuation correction," *EJNMMI Phys.*, vol. 5, p. 24, Dec. 2018.

[31] X. Dong *et al.*, "Synthetic CT generation from non-attenuation corrected PET images for whole-body PET imaging," *Phys. Med. Biol.*, vol. 64, no. 21, 2019, Art. no. 215016.

[32] X. Dong *et al.*, "Deep learning-based attenuation correction in the absence of structural information for whole-body positron emission tomography imaging," *Phys. Med. Biol.*, vol. 65, no. 5, 2020, Art. no. 055011.

[33] K. Armanious *et al.*, "Independent brain ^{18}F-FDG PET attenuation correction using a deep learning approach with generative adversarial networks," *Hellenic J. Nucl. Med.*, vol. 22, no. 3, pp. 179–186, 2019.

[34] A. Torrado-Carvajal *et al.*, "Dixon-VIBE deep learning (DIVIDE) pseudo-CT synthesis for pelvis PET/MR attenuation correction," *J. Nucl. Med.*, vol. 60, no. 3, pp. 429–435, 2019.

[35] A. P. Leynes *et al.*, "Zero-echo-time and Dixon deep pseudo-CT (ZeDD CT): Direct generation of pseudo-CT images for pelvic PET/MRI attenuation correction using deep convolutional neural networks with multiparametric MRI," *J. Nucl. Med.*, vol. 59, no. 5, pp. 852–858, 2018.

[36] C. N. Ladefoged, L. Marner, A. Hindsholm, I. Law, L. Hojgaard, and F. L. Andersen, "Deep learning based attenuation correction of PET/MRI in pediatric brain tumor patients: Evaluation in a clinical setting," *Front Neurosci.*, vol. 12, p. 1005, Jan. 2019.

[37] H. Jang, F. Liu, G. Zhao, T. Bradshaw, and A. B. McMillan, "Deep learning based MRAC using rapid ultrashort echo time imaging," *Med. Phys.*, vol. 45, no. 8, pp. 3697–3704, 2018.

[38] K. D. Spuhler, J. Gardus, Y. Gao, C. DeLorenzo, R. Parsey, and C. Huang, "Synthesis of patient-specific transmission data for PET attenuation correction for PET/MRI neuroimaging using a convolutional neural network," *J. Nucl. Med.*, vol. 60, no. 4, pp. 555–560, 2019.

[39] D. Nie *et al.*, "Medical image synthesis with context-aware generative adversarial networks," in *Proc. Med. Image Comput. Comput. Assist. Intervention*, 2017, pp. 417–425.

[40] D. Nie, X. Cao, Y. Gao, L. Wang, and D. Shen, "Estimating CT image from MRI data using 3D fully convolutional networks," in *Deep Learning and Data Labeling for Medical Applications*. Cham, Switzerland: Springer, 2016, pp. 170–178.

[41] F. Liu, H. Jang, R. Kijowski, T. Bradshaw, and A. B. McMillan, "Deep learning MR imaging-based attenuation correction for PET/MR imaging," *Radiology*, vol. 286, no. 2, pp. 676–684, 2018.

[42] X. Han, "MR-based synthetic CT generation using a deep convolutional neural network method," *Med. Phys.*, vol. 44, no. 4, pp. 1408–1419, 2017.

[43] T. J. Bradshaw, G. Zhao, H. Jang, F. Liu, and A. B. McMillan, "Feasibility of deep learning-based PET/MR attenuation correction in the pelvis using only diagnostic MR images," *Tomography*, vol. 4, no. 3, pp. 138–147, 2018.

[44] H. Arabi, G. Zeng, G. Zheng, and H. Zaidi, "Novel adversarial semantic structure deep learning for MRI-guided attenuation correction in brain PET/MRI," *Eur. J. Nucl. Med. Mol. Imag.*, vol. 46, no. 13, pp. 2746–2759, 2019.

[45] A. S. Ribeiro, E. R. Kops, H. Herzog, and P. Almeida, "Hybrid approach for attenuation correction in PET/MR scanners," *Nucl. Instrum. Methods A*, vol. 734, pp. 166–170, 2014.

[46] M. Hofmann *et al.*, "MRI-based attenuation correction for whole-body PET/MRI: Quantitative evaluation of segmentation- and atlas-based methods," *J. Nucl. Med.*, vol. 52, no. 9, pp. 1392–1399, Sep, 2011.

[47] M. Hofmann *et al.*, "MRI-based attenuation correction for PET/MRI: A novel approach combining pattern recognition and atlas registration," *J. Nucl. Med.*, vol. 49, no. 11, pp. 1875–1883, 2008.

[48] S. K. Yu and C. Nahmias, "Segmented attenuation correction using artificial neural networks in positron tomography," *Phys. Med. Biol.*, vol. 41, no. 10, pp. 2189–2206, 1996.

[49] K. Ogawa and N. Nishizaki, "Accurate scatter compensation using neural networks in radionuclide imaging," *IEEE Trans. Nucl. Sci.*, vol. 40, no. 4, pp. 1020–1025, 1993.

[50] M. T. Munley, C. E. Floyd, Jr., J. E. Bowsher, and R. E. Coleman, "An artificial neural network approach to quantitative single photon emission computed tomographic reconstruction with collimator, attenuation, and scatter compensation," *Med. Phys.*, vol. 21, no. 12, pp. 1889–1899, 1994.

[51] P. Maksud, B. Fertil, C. Rica, G. El Fakhri, and A. Aurengo, "Artificial neural network as a tool to compensate for scatter and attenuation in radionuclide imaging," *J. Nucl. Med.*, vol. 39, no. 4, pp. 735–745, 1998.

[52] L. Tao, J. Fisher, E. Anaya, X. Li, and C. S. Levin, "Pseudo CT image synthesis and bone segmentation from MR images using adversarial networks with residual blocks for MR-based attenuation correction of brain PET data," *IEEE Trans. Radiat. Plasma Med. Sci.*, early access, Apr. 21, 2020, doi: 10.1109/TRPMS.2020.2989073.

[53] S. R. Cherry and M. Dahlbom, *PET: Physics, Instrumentation, and Scanners*. New York, NY, USA: Springer, 2004.

[54] D. L. Bailey, M. N. Maisey, D. W. Townsend, and P. E. Valk, *Positron Emission Tomography: Basic Sciences*. London, U.K.: Springer, 2005.

[55] B. Bendriem and D. W. Townsend, *The Theory and Practice of 3D PET*. Dordrecht, The Netherlands: Springer, 2013.

[56] A. J. Reader and H. Zaidi, "Advances in PET image reconstruction," *PET Clin.*, vol. 2, no. 2, pp. 173–190, 2007.

[57] H. Zaidi and M. L. Montandon, "Scatter compensation techniques in PET," *PET Clin.*, vol. 2, no. 2, pp. 219–234, 2007.

[58] I. Goodfellow, Y. Bengio, and A. Courville, *Deep Learning*, Cambridge, MA, USA: MIT Press, 2016.

[59] Y. LeCun, Y. Bengio, and G. Hinton, "Deep learning," *Nature*, vol. 521, no. 7553, pp. 436–444, 2015.

[60] D. Shen, G. Wu, and H.-I. Suk, "Deep learning in medical image analysis," *Annu. Rev. Biomed. Eng.*, vol. 19, pp. 221–248, Jun. 2017.

[61] C. M. Bishop, *Pattern Recognition and Machine Learning*. New York, NY, USA: Springer, 2006.

[62] R. Accorsi, L. E. Adam, M. E. Werner, and J. S. Karp, "Optimization of a fully 3D single scatter simulation algorithm for 3D PET," *Phys. Med. Biol.*, vol. 49, no. 12, pp. 2577–2598, 2004.

[63] J. M. Ollinger, "Model-based scatter correction for fully 3D PET," *Phys. Med. Biol.*, vol. 41, no. 1, pp. 153–176, 1996.

[64] C. C. Watson, "New, faster, image-based scatter correction for 3D PET," *IEEE Trans. Nucl. Sci.*, vol. 47, no. 4, pp. 1587–1594, Aug. 2000.

[65] S. Wollenweber, "Parameterization of a model-based 3-D PET scatter correction," *IEEE Trans. Nucl. Sci.*, vol. 49, no. 3, pp. 722–727, Jun. 2002.

[66] E. Z. Xu, N. A. Mullani, K. L. Gould, and W. Anderson, "A segmented attenuation correction for PET," *J. Nucl. Med.*, vol. 32, no. 1, pp. 161–165, 1991.

[67] M. Bergström, J. Litton, L. Eriksson, C. Bohm, and G. Blomqvist, "Determination of object contour from projections for attenuation correction in cranial positron emission tomography," *J. Comput. Assist. Tomography*, vol. 6, no. 2, pp. 365–372, 1982.

[68] S. Siegel and M. Dahlbom, "Implementation and evaluation of a calculated attenuation correction for PET," *IEEE Trans. Nucl. Sci.*, vol. 39, no. 4, pp. 1117–1121, Aug. 1992.

[69] P. K. Hooper, S. R. Meikle, S. Eberl, and M. J. Fulham, "Validation of postinjection transmission measurements for attenuation correction in neurological FDG-PET studies," *J. Nucl. Med.*, vol. 37, no. 1, pp. 128–136, 1996.

[70] K. Kaneko *et al.*, "Validation of quantitative accuracy of the post-injection transmission-based and transmissionless attenuation correction techniques in neurological FDG-PET," *Nucl. Med. Commun.*, vol. 25, no. 11, pp. 1095–1102, 2004.

[71] W. Sureshbabu and O. Mawlawi, "PET/CT imaging artifacts," *J. Nucl. Med. Technol.*, vol. 33, no. 3, pp. 156–161, 2005.

[72] T. Beyer, A. Bockisch, H. Kühl, and M.-J. Martinez, "Whole-body 18F-FDG PET/CT in the presence of truncation artifacts," *J. Nucl. Med.*, vol. 47, no. 1, pp. 91–99, 2006.

[73] O. Mawlawi *et al.*, "Truncation artifact on PET/CT: Impact on measurements of activity concentration and assessment of a correction algorithm," *AJR Amer. J. Roentgenol.*, vol. 186, no. 5, pp. 1458–1467, 2006.

[74] C. R. Hunter, R. Klein, R. S. Beanlands, and R. A. deKemp, "Patient motion effects on the quantification of regional myocardial blood flow with dynamic PET imaging," *Med. Phys.*, vol. 43, no. 4, p. 1829, 2016.

[75] M. A. Lodge, J. C. Mhlanga, S. Y. Cho, and R. L. Wahl, "Effect of patient arm motion in whole-body PET/CT," *J. Nucl. Med.*, vol. 52, no. 12, pp. 1891–1897, 2011.

[76] A. Martinez-Möller, M. Souvatzoglou, N. Navab, M. Schwaiger, and S. G. Nekolla, "Artifacts from misaligned CT in cardiac perfusion PET/CT studies: frequency, effects, and potential solutions," *J. Nucl. Med.*, vol. 48, no. 2, pp. 188–193, 2007.

[77] A. M. Alessio, S. Kohlmyer, K. Branch, G. Chen, J. Caldwell, and P. Kinahan, "Cine CT for attenuation correction in cardiac PET/CT," *J. Nucl. Med.*, vol. 48, no. 5, pp. 794–801, 2007.

[78] T. Pan *et al.*, "Attenuation correction of PET images with respiration-averaged CT images in PET/CT," *J. Nucl. Med.*, vol. 46, no. 9, pp. 1481–1487, 2005.

[79] B. J. Pichler, A. Kolb, T. Nägele, and H.-P. Schlemmer, "PET/MRI: Paving the way for the next generation of clinical multimodality imaging applications," *J. Nucl. Med.*, vol. 51, no. 3, pp. 333–336, 2010.

[80] G. Delso *et al.*, "Performance measurements of the Siemens mMR integrated whole-body PET/MR scanner," *J. Nucl. Med.*, vol. 52, no. 12, pp. 1914–1922, 2011.

[81] C. S. Levin, S. H. Maramraju, M. M. Khalighi, T. W. Deller, G. Delso, and F. Jansen, "Design features and mutual compatibility studies of the time-of-flight PET capable GE SIGNA PET/MR system," *IEEE Trans. Med. Imag.*, vol. 35, no. 8, pp. 1907–1914, Aug. 2016.

[82] H. Zaidi *et al.*, "Design and performance evaluation of a whole-body Ingenuity TF PET–MRI system," *Phys. Med. Biol.*, vol. 56, no. 10, p. 3091, 2011.

[83] S. Balyasnikova *et al.*, "PET/MR in oncology: an introduction with focus on MR and future perspectives for hybrid imaging," *Amer. J. Nucl. Med. Mol. Imag.*, vol. 2, no. 4, pp. 458–474, 2012.

[84] F. C. Gaertner *et al.*, "Evaluation of feasibility and image quality of 68Ga-DOTATOC positron emission tomography/magnetic resonance in comparison with positron emission tomography/computed tomography in patients with neuroendocrine tumors," *Invest. Radiol.*, vol. 48, no. 5, pp. 263–272, 2013.

[85] C. Gaeta, J. Vercher-Conejero, A. Sher, A. Kohan, C. Rubbert, and N. Avril, "Recurrent and metastatic breast cancer PET, PET/CT, PET/MRI: FDG and new biomarkers," *Q J. Nucl. Med. Mol. Imag.*, vol. 57, no. 4, pp. 352–366, 2013.

[86] I. Jambor *et al.*, "Improved detection of localized prostate cancer using co-registered MRI and 11C-acetate PET/CT," *Eur. J. Radiol.*, vol. 81, no. 11, pp. 2966–2972, 2012.

[87] K. Kubiessa *et al.*, "Initial clinical results of simultaneous 18 F-FDG PET/MRI in comparison to 18 F-FDG PET/CT in patients with head and neck cancer," *Eur. J. Nucl. Med. Mol. Imag.*, vol. 41, no. 4, pp. 639–648, 2014.

[88] T. Takei *et al.*, "A case of multimodality multiparametric 11C-choline PET/MR for biopsy targeting in prior biopsy-negative primary prostate cancer," *Clin. Nucl. Med.*, vol. 37, no. 9, pp. 918–919, 2012.

[89] C. Catana *et al.*, "Simultaneous in vivo positron emission tomography and magnetic resonance imaging," *Proc. Nat. Acad. Sci. USA*, vol. 105, no. 10, pp. 3705–3710, 2008.

[90] M. S. Judenhofer *et al.*, "Simultaneous PET-MRI: A new approach for functional and morphological imaging," *Nat. Med.*, vol. 14, no. 4, pp. 459–465, 2008.

[91] G. B. Ko *et al.*, "Simultaneous multiparametric PET/MRI with silicon photomultiplier PET and ultra-high-field MRI for small-animal imaging," *J. Nucl. Med.*, vol. 57, no. 8, pp. 1309–1315, 2016.

[92] J. Wehner *et al.*, "MR-compatibility assessment of the first preclinical PET-MRI insert equipped with digital silicon photomultipliers," *Phys. Med. Biol.*, vol. 60, no. 6, pp. 2231–2255, 2015.

[93] H. S. Yoon *et al.*, "Initial results of simultaneous PET/MRI experiments with an MRI-compatible silicon photomultiplier PET scanner," *J. Nucl. Med.*, vol. 53, no. 4, pp. 608–614, 2012.

[94] S. Y. Chun *et al.*, "MRI-based nonrigid motion correction in simultaneous PET/MRI," *J. Nucl. Med.*, vol. 53, no. 8, pp. 1284–1291, 2012.

[95] C. Y. Sander *et al.*, "Neurovascular coupling to D2/D3 dopamine receptor occupancy using simultaneous PET/functional MRI," *Proc. Nat. Acad. Sci. USA*, vol. 110, no. 27, pp. 11169–11174, 2013.

[96] H. F. Wehrl *et al.*, "Simultaneous PET-MRI reveals brain function in activated and resting state on metabolic, hemodynamic and multiple temporal scales," *Nat. Med.*, vol. 19, no. 9, pp. 1184–1189, 2013.

[97] C. Würslin *et al.*, "Respiratory motion correction in oncologic PET using T1-weighted MR imaging on a simultaneous whole-body PET/MR system," *J. Nucl. Med.*, vol. 54, no. 3, pp. 464–471, 2013.

[98] M. Hofmann, B. Pichler, B. Schölkopf, and T. Beyer, "Towards quantitative PET/MRI: A review of MR-based attenuation correction techniques," *Eur. J. Nucl. Med. Mol. Imag.*, vol. 36, no. 1, pp. 93–104, 2009.

[99] Y. Berker *et al.*, "MRI-based attenuation correction for hybrid PET/MRI systems: A 4-class tissue segmentation technique using a combined ultrashort-echo-time/Dixon MRI sequence," *J. Nucl. Med.*, vol. 53, no. 5, pp. 796–804, 2012.

[100] M. Eiber *et al.*, "Value of a Dixon-based MR/PET attenuation correction sequence for the localization and evaluation of PET-positive lesions," *Eur. J. Nucl. Med. Mol. Imag.*, vol. 38, no. 9, pp. 1691–1701, 2011.

[101] A. Martinez-Möller *et al.*, "Tissue classification as a potential approach for attenuation correction in whole-body PET/MRI: Evaluation with PET/CT data," *J. Nucl. Med.*, vol. 50, no. 4, pp. 520–526, 2009.

[102] J. Ma, "Dixon techniques for water and fat imaging," *J. Mag. Reson. Imag.*, vol. 28, no. 3, pp. 543–558, 2008.

[103] V. Keereman, P. Mollet, Y. Berker, V. Schulz, and S. Vandenberghe, "Challenges and current methods for attenuation correction in PET/MR," *Mag. Reson. Mater. Phy.*, vol. 26, no. 1, pp. 81–98, 2013.

[104] H. R. Marshall, F. S. Prato, L. Deans, J. Théberge, R. T. Thompson, and R. Z. Stodilka, "Variable lung density consideration in attenuation correction of whole-body PET/MRI," *J. Nucl. Med.*, vol. 53, no. 6, pp. 977–984, 2012.

[105] V. Schulz *et al.*, "Automatic, three-segment, MR-based attenuation correction for whole-body PET/MR data," *Eur. J. Nucl. Med. Mol. Imag.*, vol. 38, no. 1, pp. 138–152, 2011.

[106] D. Izquierdo-Garcia *et al.*, "Comparison of MR-based attenuation correction and CT-based attenuation correction of whole-body PET/MR imaging," *Eur. J. Nucl. Med. Mol. Imag.*, vol. 41, no. 8, pp. 1574–1584, 2014.

[107] J. H. Kim, J. S. Lee, I.-C. Song, and D. S. Lee, "Comparison of segmentation-based attenuation correction methods for PET/MRI: Evaluation of bone and liver standardized uptake value with oncologic PET/CT data," *J. Nucl. Med.*, vol. 53, no. 12, pp. 1878–1882, 2012.

[108] M. Hofmann *et al.*, "MRI-based attenuation correction for whole-body PET/MRI: Quantitative evaluation of segmentation-and atlas-based methods," *J. Nucl. Med.*, vol. 52, no. 9, pp. 1392–1399, 2011.

[109] A. Samarin *et al.*, "PET/MR imaging of bone lesions–implications for PET quantification from imperfect attenuation correction," *Eur. J. Nucl. Med. Mol. Imag.*, vol. 39, no. 7, pp. 1154–1160, 2012.

[110] D. H. Paulus *et al.*, "Whole-body PET/MR imaging: Quantitative evaluation of a novel model-based MR attenuation correction method including bone," *J. Nucl. Med.*, vol. 56, no. 7, pp. 1061–1066, 2015.

[111] I. Rausch, H. H. Quick, J. Cal-Gonzalez, B. Sattler, R. Boellaard, and T. Beyer, "Technical and instrumentational foundations of PET/MRI," *Eur. J. Radiol.*, vol. 94, pp. A3–A13, Sep. 2017.

[112] J. Tang *et al.*, "Effect of MR truncation compensation on quantitative PET image reconstruction for whole-body PET/MR," in *Proc. IEEE Nucl. Sci. Symp. Conf. Rec.*, 2011, pp. 2506–2509.

[113] J. Nuyts, G. Bal, F. Kehren, M. Fenchel, C. Michel, and C. Watson, "Completion of a truncated attenuation image from the attenuated PET emission data," *IEEE Trans. Med. Imag.*, vol. 32, no. 2, pp. 237–246, Feb. 2012.

[114] N. Fuin *et al.*, "PET/MRI in the presence of metal implants: completion of the attenuation map from PET emission data," *J. Nucl. Med.*, vol. 58, no. 5, pp. 840–845, 2017.

[115] T. Heu, C. M. Rank, Y. Berker, M. T. Freitag, and M. Kachelrieß, "MLAA-based attenuation correction of flexible hardware components in hybrid PET/MR imaging," *EJNMMI Phys.*, vol. 4, no. 1, p. 12, 2017.

[116] M. E. Lindemann, M. Oehmigen, J. O. Blumhagen, M. Gratz, and H. H. Quick, "MR-based truncation and attenuation correction in integrated PET/MR hybrid imaging using HUGE with continuous table motion," *Med. Phys.*, vol. 44, no. 9, pp. 4559–4572, 2017.

[117] L. B. Aasheim *et al.*, "PET/MR brain imaging: Evaluation of clinical UTE-based attenuation correction," *Eur. J. Nucl. Med. Mol. Imag.*, vol. 42, no. 9, pp. 1439–1446, 2015.

[118] A. Aitken *et al.*, "Improved UTE-based attenuation correction for cranial PET-MR using dynamic magnetic field monitoring," *Med. Phys.*, vol. 41, no. 1, 2014, Art. no. 012302.

[119] H. J. An *et al.*, "MRI-based attenuation correction for PET/MRI using multiphase level-set method," *J. Nucl. Med.*, vol. 57, no. 4, pp. 587–593, 2016.

[120] J. Cabello, M. Lukas, S. Förster, T. Pyka, S. G. Nekolla, and S. I. Ziegler, "MR-based attenuation correction using ultrashort-echo-time pulse sequences in dementia patients," *J. Nucl. Med.*, vol. 56, no. 3, pp. 423–429, 2015.

[121] C. Catana *et al.*, "Toward implementing an MRI-based PET attenuation-correction method for neurologic studies on the MR-PET brain prototype," *J. Nucl. Med.*, vol. 51, no. 9, pp. 1431–1438, 2010.

[122] M. R. Juttukonda *et al.*, "MR-based attenuation correction for PET/MRI neurological studies with continuous-valued attenuation coefficients for bone through a conversion from R2* to CT-Hounsfield units," *Neuroimage*, vol. 112, pp. 160–168, May 2016.

[123] V. Keereman, Y. Fierens, T. Broux, Y. De Deene, M. Lonneux, and S. Vandenberghe, "MRI-based attenuation correction for PET/MRI using ultrashort echo time sequences," *J. Nucl. Med.*, vol. 51, no. 5, pp. 812–818, 2010.

[124] C. N. Ladefoged *et al.*, "Region specific optimization of continuous linear attenuation coefficients based on UTE (RESOLUTE): Application to PET/MR brain imaging," *Phys. Med. Biol.*, vol. 60, no. 20, pp. 8047–8065, 2015.

[125] B. K. Navalpakkam, H. Braun, T. Kuwert, and H. H. Quick, "Magnetic resonance–based attenuation correction for PET/MR hybrid imaging using continuous valued attenuation maps," *Invest. Radiol.*, vol. 48, no. 5, pp. 323–332, 2013.

[126] G. Delso, B. Fernandez, F. Wiesinger, Y. Jian, C. Bobb, and F. Jansen, "Repeatability of ZTE bone maps of the head," *IEEE Trans. Radiat. Plasma Med. Sci.*, vol. 2, no. 3, pp. 244–249, May 2018.

[127] G. Delso *et al.*, "Clinical evaluation of zero-echo-time MR imaging for the segmentation of the skull," *J. Nucl. Med.*, vol. 56, no. 3, pp. 417–422, 2015.

[128] A. P. Leynes *et al.*, "Hybrid ZTE/Dixon MR-based attenuation correction for quantitative uptake estimation of pelvic lesions in PET/MRI," *Med. Phys.*, vol. 44, no. 3, pp. 902–913, 2017.

[129] B. Sgard *et al.*, "ZTE MR-based attenuation correction in brain FDG-PET/MR: Performance in patients with cognitive impairment," *Eur. Radiol.*, vol. 30, no. 3, pp. 1770–1779, 2020.

[130] F. Wiesinger *et al.*, "Zero TE MR bone imaging in the head," *Mag. Reson. Med.*, vol. 75, no. 1, pp. 107–114, 2016.

[131] J. Yang *et al.*, "Evaluation of sinus/edge-corrected zero-echo-time-based attenuation correction in brain PET/MRI," *J. Nucl. Med.*, vol. 58, no. 11, pp. 1873–1879, 2017.

[132] A. Boss, M. Weiger, and F. Wiesinger, "Future image acquisition trends for PET/MRI," *Seminars Nucl. Med.*, vol. 45, no. 3, pp. 201–211, 2015.

[133] J. Du, M. Carl, M. Bydder, A. Takahashi, C. B. Chung, and G. M. Bydder, "Qualitative and quantitative ultrashort echo time (UTE) imaging of cortical bone," *J. Mag. Reson.*, vol. 207, no. 2, pp. 304–311, 2010.

[134] M. D. Robson, P. D. Gatehouse, M. Bydder, and G. M. Bydder, "Magnetic resonance: An introduction to ultrashort TE (UTE) imaging," *J. Comput. Assist. Tomography*, vol. 27, no. 6, pp. 825–846, 2003.

[135] H. Choi *et al.*, "Segmentation-based MR attenuation correction including bones also affects quantitation in brain studies: An initial result of 18F-FP-CIT PET/MR for patients with parkinsonism," *J. Nucl. Med.*, vol. 55, no. 10, pp. 1617–1622, 2014.

[136] J. C. Dickson, C. O'Meara, and A. Barnes, "A comparison of CT-and MR-based attenuation correction in neurological PET," *Eur. J. Nucl. Med. Mol. Imag.*, vol. 41, no. 6, pp. 1176–1189, 2014.

[137] R. E. Breighner, Y. Endo, G. P. Konin, L. V. Gulotta, M. F. Koff, and H. G. Potter, "Zero echo time imaging of the shoulder: Enhanced osseous detail by using MR imaging," *Radiology*, vol. 286, no. 3, pp. 960–966, 2018.

[138] M. Weiger and K. Pruessmann, "MRI with zero echo time," *eMagRes*, vol. 1, no. 2, pp. 311–322, 2012.

[139] G. Delso, D. Gillett, W. Bashari, T. Matys, I. Mendichovszky, and M. Gurnell, "Clinical evaluation of ^{11}C-Met-Avid pituitary lesions using a ZTE-based AC method," *IEEE Trans. Radiat. Plasma Med. Sci.*, vol. 3, no. 4, pp. 504–508, Jul. 2019.

[140] D. Izquierdo-Garcia, M. C. Eldaief, M. G. Vangel, and C. Catana, "Intrascanner reproducibility of an SPM-based head MR-based attenuation correction method," *IEEE Trans. Radiat. Plasma Med. Sci.*, vol. 3, no. 3, pp. 327–333, May 2019.

[141] N. Burgos *et al.*, "Attenuation correction synthesis for hybrid PET-MR scanners: Application to brain studies," *IEEE Trans. Med. Imag.*, vol. 33, no. 12, pp. 2332–2341, Dec. 2014.

[142] Y. Chen *et al.*, "Probabilistic air segmentation and sparse regression estimated pseudo CT for PET/MR attenuation correction," *Radiology*, vol. 275, no. 2, pp. 562–569, 2015.

[143] D. Izquierdo-Garcia *et al.*, "An SPM8-based approach for attenuation correction combining segmentation and nonrigid template formation: application to simultaneous PET/MR brain imaging," *J. Nucl. Med.*, vol. 55, no. 11, pp. 1825–1830, 2014.

[144] E. R. Kops and H. Herzog, "Alternative methods for attenuation correction for PET images in MR-PET scanners," in *Proc. IEEE Nucl. Sci. Symp. Conf. Rec.*, vol. 6, 2007, pp. 4327–4330.

[145] I. Merida, A. Reilhac, J. Redoute, R. A. Heckemann, N. Costes, and A. Hammers, "Multi-atlas attenuation correction supports full quantification of static and dynamic brain PET data in PET-MR," *Phys. Med. Biol.*, vol. 62, no. 7, pp. 2834–2858, 2017.

[146] E. Schreibmann, J. A. Nye, D. M. Schuster, D. R. Martin, J. Votaw, and T. Fox, "MR-based attenuation correction for hybrid PET-MR brain imaging systems using deformable image registration," *Med. Phys.*, vol. 37, no. 5, pp. 2101–2109, 2010.

[147] T. Sekine *et al.*, "Evaluation of atlas-based attenuation correction for integrated PET/MR in human brain: Application of a head atlas and comparison to true CT-based attenuation correction," *J. Nucl. Med.*, vol. 57, no. 2, pp. 215–220, 2016.

[148] T. Sekine *et al.*, "Multi-atlas-based attenuation correction for brain 18F-FDG PET imaging using a time-of-flight PET/MR scanner: Comparison with clinical single-atlas- and CT-based attenuation correction," *J. Nucl. Med.*, vol. 57, no. 8, pp. 1258–1264, 2016.

[149] M. Eldib, J. Bini, D. D. Faul, N. Oesingmann, C. Tsoumpas, and Z. A. Fayad, "Attenuation correction for magnetic resonance coils in combined PET/MR imaging: A review," *PET Clin.*, vol. 11, no. 2, pp. 151–160, 2016.

[150] D. H. Paulus, H. Braun, B. Aklan, and H. H. Quick, "Simultaneous PET/MR imaging: MR-based attenuation correction of local radiofrequency surface coils," *Med. Phys.*, vol. 39, no. 7, pp. 4306–4315, 2012.

[151] C. Y. Sander, B. Keil, D. B. Chonde, B. R. Rosen, C. Catana, and L. L. Wald, "A 31-channel MR brain array coil compatible with positron emission tomography," *Mag. Reson. Med.*, vol. 73, no. 6, pp. 2363–2375, 2015.

[152] H. A. Archer *et al.*, "Amyloid load and cerebral atrophy in Alzheimer's disease: an 11C-PIB positron emission tomography study," *Ann. Neurol.*, vol. 60, no. 1, pp. 145–147, 2006.

[153] H. Cho *et al.*, "Tau PET in Alzheimer disease and mild cognitive impairment," *Neurology*, vol. 87, no. 4, pp. 375–383, 2016.

[154] S. Jin *et al.*, "Differential diagnosis of parkinsonism using dual-phase F-18 FP-CIT PET imaging," *Nucl. Med. Mol. Imag.*, vol. 47, no. 1, pp. 44–51, 2013.

[155] L. Kerenyi *et al.*, "Positron emission tomography of striatal serotonin transporters in Parkinson disease," *Archives Neurol.*, vol. 60, no. 9, pp. 1223–1229, 2003.

[156] H. Tashima *et al.*, "First prototyping of a dedicated PET system with the hemisphere detector arrangement," *Phys. Med. Biol.*, vol. 64, no. 6, 2019, Art. no. 065004.

[157] A. M. Ahmed, H. Tashima, E. Yoshida, F. Nishikido, and T. Yamaya, "Simulation study comparing the helmet-chin PET with a cylindrical PET of the same number of detectors," *Phys. Med. Biol.*, vol. 62, no. 11, pp. 4541–4550, 2017.

[158] C. E. Bauer *et al.*, "Concept of an upright wearable positron emission tomography imager in humans," *Brain Behav.*, vol. 6, no. 9, 2016, Art. no. e00530.

[159] S. Yamamoto, M. Honda, T. Oohashi, K. Shimizu, and M. Senda, "Development of a brain PET system, PET-Hat: A wearable PET system for brain research," *IEEE Trans. Nucl. Sci.*, vol. 58, no. 3, pp. 668–673, Jun. 2011.

[160] J. Park, D. Hwang, K. Y. Kim, S. K. Kang, Y. K. Kim, and J. S. Lee, "Computed tomography super-resolution using deep convolutional neural network," *Phys. Med. Biol.*, vol. 63, no. 14, 2018, Art. no. 145011.

[161] H. Chen *et al.*, "Low-dose CT with a residual encoder–decoder convolutional neural network," *IEEE Trans. Med. Imag.*, vol. 36, no. 12, pp. 2524–2535, Dec. 2017.

[162] E. Kang, J. Min, and J. C. Ye, "A deep convolutional neural network using directional wavelets for low-dose X-ray CT reconstruction," *Med. Phys.*, vol. 44, no. 10, pp. e360–e375, 2017.

[163] J. S. Karp, S. Surti, M. E. Daube-Witherspoon, and G. Muehllehner, "Benefit of time-of-flight in PET: Experimental and clinical results," *J. Nucl. Med.*, vol. 49, no. 3, pp. 462–470, 2008.

[164] S. Vandenberghe, E. Mikhaylova, E. D'Hoe, P. Mollet, and J. S. Karp, "Recent developments in time-of-flight PET," *EJNMMI Phys.*, vol. 3, p. 3, Dec. 2016.

[165] T. K. Lewellen, "Time-of-flight PET," *Seminars Nucl. Med.*, vol. 28, no. 3, pp. 268–275, 1998.

[166] Y. Li, S. Matej, and J. S. Karp, "Practical joint reconstruction of activity and attenuation with autonomous scaling for time-of-flight PET," *Phys. Med. Biol.*, Apr. 2020, doi: 10.1088/1361-6560/ab8d75.

[167] M. Conti, "State of the art and challenges of time-of-flight PET," *Phys. Med.*, vol. 25, no. 1, pp. 1–11, 2009.

[168] J. W. Son *et al.*, "Proof-of-concept prototype time-of-flight PET system based on high-quantum-efficiency multianode PMTs," *Med. Phys.*, vol. 44, no. 10, pp. 5314–5324, 2017.

[169] M. Conti, "Focus on time-of-flight PET: The benefits of improved time resolution," *Eur. J. Nucl. Med. Mol. Imag.*, vol. 38, no. 6, pp. 1147–1157, 2011.

[170] P. Mollet, V. Keereman, J. Bini, D. Izquierdo-Garcia, Z. A. Fayad, and S. Vandenberghe, "Improvement of attenuation correction in time-of-flight PET/MR imaging with a positron-emitting source," *J. Nucl. Med.*, vol. 55, no. 2, pp. 329–336, 2014.

[171] H. Rothfuss *et al.*, "LSO background radiation as a transmission source using time of flight," *Phys. Med. Biol.*, vol. 59, no. 18, pp. 5483–5500, 2014.

[172] S. Y. Chun, K. Y. Kim, J. S. Lee, and J. A. Fessier, "Joint estimation of activity distribution and attenuation map for TOF-PET using alternating direction method of multiplier," in *Proc. IEEE Int. Symp. Biomed. Imag.*, 2016, pp. 86–89.

[173] M. Defrise, A. Rezaei, and J. Nuyts, "Time-of-flight PET data determine the attenuation sinogram up to a constant," *Phys. Med. Biol.*, vol. 57, no. 4, pp. 885–899, 2012.

[174] A. Rezaei *et al.*, "Simultaneous reconstruction of activity and attenuation in time-of-flight PET," *IEEE Trans. Med. Imag.*, vol. 31, no. 12, pp. 2224–2233, Dec. 2012.

[175] A. Salomon, A. Goedicke, B. Schweizer, T. Aach, and V. Schulz, "Simultaneous reconstruction of activity and attenuation for PET/MR," *IEEE Trans. Med. Imag.*, vol. 30, no. 3, pp. 804–813, Mar. 2011.

[176] M. Defrise, A. Rezaei, and J. Nuyts, "Transmission-less attenuation correction in time-of-flight PET: analysis of a discrete iterative algorithm," *Phys. Med. Biol.*, vol. 59, no. 4, pp. 1073–1095, 2014.

[177] A. Rezaei, M. Defrise, and J. Nuyts, "ML-reconstruction for TOF-PET with simultaneous estimation of the attenuation factors," *IEEE Trans. Med. Imag.*, vol. 33, no. 7, pp. 1563–1572, Jul. 2014.

[178] A. Rezaei, G. Schramm, S. M. A. Willekens, G. Delso, K. Van Laere, and J. Nuyts, "A quantitative evaluation of joint activity and attenuation reconstruction in TOF PET/MR brain imaging," *J. Nucl. Med.*, vol. 60, no. 11, pp. 1649–1655, 2019.
[179] S. Ahn *et al.*, "Joint estimation of activity and attenuation for PET using pragmatic MR-based prior: Application to clinical TOF PET/MR whole-body data for FDG and non-FDG tracers," *Phys. Med. Biol.*, vol. 63, no. 4, 2018, Art. no. 045006.
[180] A. Mehranian and H. Zaidi, "Joint estimation of activity and attenuation in whole-body TOF PET/MRI using constrained Gaussian mixture models," *IEEE Trans. Med. Imag.*, vol. 34, no. 9, pp. 1808–1821, Sep. 2015.
[181] S. Wang and R. M. Summers, "Machine learning and radiology," *Med. Image. Anal.*, vol. 16, no. 5, pp. 933–951, 2012.
[182] T. Nochino, Y. Ohno, T. Kato, M. Taniike, and S. Okada, "Sleep stage estimation method using a camera for home use," *Biomed. Eng. Lett.*, vol. 9, no. 2, pp. 257–265, 2019.
[183] A. Yonekura, H. Kawanaka, V. B. S. Prasath, B. J. Aronow, and H. Takase, "Automatic disease stage classification of glioblastoma multiforme histopathological images using deep convolutional neural network," *Biomed. Eng. Lett.*, vol. 8, no. 3, pp. 321–327, 2018.
[184] F. Nensa, A. Demircioglu, and C. Rischpler, "Artificial intelligence in nuclear medicine," *J. Nucl. Med.*, vol. 60, no. S2, pp. 29s–37s, 2019.
[185] C. Park, C. C. Took, and J. K. Seong, "Machine learning in biomedical engineering," *Biomed. Eng. Lett.*, vol. 8, no. 1, pp. 1–3, 2018.
[186] J. H. Lee, Y. J. Kim, and K. G. Kim, "Bone age estimation using deep learning and hand X-ray images," *Biomed. Eng. Lett.*, Mar. 2020, doi: 10.1007/s13534-020-00151-y.
[187] A. H. Shahid and M. P. Singh, "A deep learning approach for prediction of Parkinson's disease progression," *Biomed. Eng. Lett.*, vol. 10, no. 2, pp. 227–239, 2020.
[188] J.-B. Michaud *et al.*, "Sensitivity increase through a neural network method for LOR recovery of ICS triple coincidences in high-resolution pixelated-detectors PET scanners," *IEEE Trans. Nucl. Sci.*, vol. 62, no. 1, pp. 82–94, Feb. 2014.
[189] Y. Wang, W. Zhu, X. Cheng, and D. Li, "3D position estimation using an artificial neural network for a continuous scintillator PET detector," *Phys. Med. Biol.*, vol. 58, no. 5, pp. 1375–1390, 2013.
[190] J. S. Lee, D. D. Lee, S. Choi, K. S. Park, and D. S. Lee, "Non-negative matrix factorization of dynamic images in nuclear medicine," in *Proc. IEEE Nucl. Sci. Symp. Conf. Rec.*, vol. 4, 2001, pp. 2027–2030.
[191] J. S. Lee *et al.*, "Blind separation of cardiac components and extraction of input function from H215O dynamic myocardial PET using independent component analysis," *J. Nucl. Med.*, vol. 42, no. 6, pp. 938–943, 2001.
[192] M. Naganawa, Y. Kimura, K. Ishii, K. Oda, K. Ishiwata, and A. Matani, "Extraction of a plasma time-activity curve from dynamic brain PET images based on independent component analysis," *IEEE Trans. Biomed. Eng.*, vol. 52, no. 2, pp. 201–210, Feb. 2005.
[193] K. H. Su, L. C. Wu, R. S. Liu, S. J. Wang, and J. C. Chen, "Quantification method in [18F]fluorodeoxyglucose brain positron emission tomography using independent component analysis," *Nucl. Med. Commun.*, vol. 26, no. 11, pp. 995–1004, 2005.
[194] S. Shrestha and P. P. Sengupta, "Machine learning for nuclear cardiology: The way forward," *J. Nucl. Cardiol.*, vol. 26, no. 5, pp. 1755–1758, 2019.
[195] D. Visvikis, C. C. Le Rest, V. Jaouen, and M. Hatt, "Artificial intelligence, machine (deep) learning and radio(geno)mics: definitions and nuclear medicine imaging applications," *Eur. J. Nucl. Med. Mol. Imag.*, vol. 46, no. 13, pp. 2630–2637, 2019.
[196] H. Choi, "Deep learning in nuclear medicine and molecular imaging: Current perspectives and future directions," *Nucl. Med. Mol. Imag.*, vol. 52, no. 2, pp. 109–118, 2018.
[197] K. T. Chen *et al.*, "Ultra–low-dose 18F-florbetaben amyloid PET imaging using deep learning with multi-contrast MRI inputs," *Radiology*, vol. 290, no. 3, pp. 649–656, 2019.
[198] Y. Wang *et al.*, "3D conditional generative adversarial networks for high-quality PET image estimation at low dose," *Neuroimage*, vol. 174, pp. 550–562, Jul. 2018.
[199] K. Kim *et al.*, "Penalized PET reconstruction using deep learning prior and local linear fitting," *IEEE Trans. Med. Imag.*, vol. 37, no. 6, pp. 1478–1487, Jun. 2018.
[200] J. Ouyang, K. T. Chen, E. Gong, J. Pauly, and G. Zaharchuk, "Ultra-low-dose PET reconstruction using generative adversarial network with feature matching and task-specific perceptual loss," *Med. Phys.*, vol. 46, no. 8, pp. 3555–3564, 2019.
[201] P. Jackson, N. Hardcastle, N. Dawe, T. Kron, M. S. Hofman, and R. J. Hicks, "Deep learning renal segmentation for fully automated radiation dose estimation in unsealed source therapy," *Front Oncol.*, vol. 8, p. 215, Jun. 2018.
[202] J. Park *et al.*, "Measurement of glomerular filtration rate using quantitative SPECT/CT and deep-learning-based kidney segmentation," *Sci. Rep.*, vol. 9, no. 1, p. 4223, 2019.
[203] S. K. Kang *et al.*, "Adaptive template generation for amyloid PET using a deep learning approach," *Human Brain Map.*, vol. 39, no. 9, pp. 3769–3778, 2018.
[204] H. Choi and D. S. Lee, "Generation of structural MR images from amyloid PET: Application to MR-less quantification," *J. Nucl. Med.*, vol. 59, no. 7, pp. 1111–1117, 2018.
[205] M. S. Lee, D. Hwang, J. H. Kim, and J. S. Lee, "Deep-dose: A voxel dose estimation method using deep convolutional neural network for personalized internal dosimetry," *Sci. Rep.*, vol. 9, no. 1, 2019, Art. no. 10308.
[206] H. I. Suk, S. W. Lee, and D. Shen, "Hierarchical feature representation and multimodal fusion with deep learning for AD/MCI diagnosis," *Neuroimage*, vol. 101, pp. 569–582, Nov. 2014.
[207] H. Choi and K. H. Jin, "Predicting cognitive decline with deep learning of brain metabolism and amyloid imaging," *Behav. Brain Res.*, vol. 344, pp. 103–109, May 2018.
[208] H. J. Son *et al.*, "The clinical feasibility of deep learning-based classification of amyloid PET images in visually equivocal cases," *Eur. J. Nucl. Med. Mol. Imag.*, vol. 47, no. 2, pp. 332–341, 2020.
[209] J. Y. Kim *et al.*, "Amyloid PET quantification via end-to-end training of a deep learning," *Nucl. Med. Mol. Imag.*, vol. 53, no. 5, pp. 340–348, 2019.
[210] M. Maspero *et al.*, "Dose evaluation of fast synthetic-CT generation using a generative adversarial network for general pelvis MR-only radiotherapy," *Phys. Med. Biol.*, vol. 63, no. 18, 2018, Art. no. 185001.
[211] A. M. Dinkla *et al.*, "MR-only brain radiation therapy: Dosimetric evaluation of synthetic CTs generated by a dilated convolutional neural network," *Int. J. Radiat. Oncol. Biol. Phys.*, vol. 102, no. 4, pp. 801–812, 2018.
[212] S. Olberg *et al.*, "Synthetic CT reconstruction using a deep spatial pyramid convolutional framework for MR-only breast radiotherapy," *Med. Phys.*, vol. 46, no. 9, pp. 4135–4147, 2019.
[213] Y. Lei *et al.*, "MRI-only based synthetic CT generation using dense cycle consistent generative adversarial networks," *Med. Phys.*, vol. 46, no. 8, pp. 3565–3581, 2019.
[214] M. A. Schmidt and G. S. Payne, "Radiotherapy planning using MRI," *Phys. Med. Biol.*, vol. 60, no. 22, pp. R323–R361, 2015.
[215] N. Tyagi *et al.*, "Clinical workflow for MR-only simulation and planning in prostate," *Radiat. Oncol.*, vol. 12, p. 119, Jul. 2017.
[216] O. Ronneberger, P. Fischer, and T. Brox, "*U*-Net: Convolutional networks for biomedical image segmentation," in *Proc. Med. Image Comput. Comput. Assist. Intervent.*, 2015, pp. 234–241.
[217] M. A. A. Hegazy, M. H. Cho, M. H. Cho, and S. Y. Lee, "*U*-net based metal segmentation on projection domain for metal artifact reduction in dental CT," *Biomed. Eng. Lett.*, vol. 9, no. 3, pp. 375–385, 2019.
[218] K. Kamnitsas *et al.*, "Efficient multi-scale 3D CNN with fully connected CRF for accurate brain lesion segmentation," *Med. Image. Anal.*, vol. 36, pp. 61–78, Feb. 2017.
[219] P. Krähenbühl and V. Koltun, "Efficient inference in fully connected CRFs with Gaussian edge potentials," in *Proc. Adv. Neural Inf. Process. Syst.*, vol. 4, 2011, pp. 109–117.
[220] B. H. Choi *et al.*, "Accurate transmission-less attenuation correction method for amyloid-β brain PET using deep neural network," in *Proc. IEEE Nucl. Sci. Symp. Med. Imag. Conf.*, 2019, Art. no. M-06-380.
[221] D. Hwang, S. K. Kang, K. Y. Kim, H. Choi, S. Seo, and J. S. Lee, "Data-driven respiratory phase-matched attenuation correction without CT," in *Proc. IEEE Nucl. Sci. Symp. Med. Imag. Conf.*, 2019, Art. no. M-15-05.
[222] J. Nuyts, A. Rezaei, and M. Defrise, "The validation problem of joint emission/transmission reconstruction from TOF-PET projections," *IEEE Trans. Radiat. Plasma Med. Sci.*, vol. 2, no. 4, pp. 273–278, Jul. 2018.
[223] Y. Ge *et al.*, "Unpaired MR to CT synthesis with explicit structural constrained adversarial learning," in *Proc. IEEE Int. Symp. Biomed. Imag.*, 2019, pp. 1096–1099.
[224] K. Gong *et al.*, "MR-based attenuation correction for brain PET using 3D cycle-consistent adversarial network," *IEEE Trans. Radiat. Plasma Med. Sci.*, early access, Jul. 3, 2020, doi: 10.1109/TRPMS.2020.3006844.

[225] S. K. Kang, H. An, E. K. Chie, J. M. Park, and J. S. Lee, "CT image prediction from weakly paired MR image using CycleGAN for dose prediction in radiotherapy," in *Proc. IEEE Nucl. Sci. Symp. Med. Imag. Conf.*, 2020.

[226] Y. Berker, J. S. Karp, and V. Schulz, "Numerical algorithms for scatter-to-attenuation reconstruction in PET: Empirical comparison of convergence, acceleration, and the effect of subsets," *IEEE Trans. Radiat. Plasma Med. Sci.*, vol. 1, no. 5, pp. 426–434, Sep. 2017.

[227] Y. Berker, F. Kiessling, and V. Schulz, "Scattered PET data for attenuation-map reconstruction in PET/MRI," *Med. Phys.*, vol. 41, no. 10, Oct. 2014, Art. no. 102502.

[228] Y. Berker and Y. Li, "Attenuation correction in emission tomography using the emission data—A review," *Med. Phys.*, vol. 43, no. 2, pp. 807–832, Feb. 2016.

[229] L. Brusaferri *et al.*, "Joint activity and attenuation reconstruction from multiple energy window data with photopeak scatter re-estimation in non-TOF 3D PET," *IEEE Trans. Radiat. Plasma Med. Sci.*, vol. 4, no. 4, pp. 410–421, Jul. 2020.

[230] D. L. Bailey and K. P. Willowson, "An evidence-based review of quantitative SPECT imaging and potential clinical applications," *J. Nucl. Med.*, vol. 54, no. 1, pp. 83–89, 2013.

[231] E. Mezzenga *et al.*, "Quantitative accuracy of 177Lu SPECT imaging for molecular radiotherapy," *PLoS ONE*, vol. 12, no. 8, 2017, Art. no. e0182888.

[232] C. F. Uribe *et al.*, "Accuracy of ^{177}Lu activity quantification in SPECT imaging: A phantom study," *EJNMMI Phys.*, vol. 4, no. 1, p. 2, 2017.

[233] W. W. Lee, "Clinical applications of technetium-99m quantitative single-photon emission computed tomography/computed tomography," *Nucl. Med. Mol. Imag.*, vol. 53, no. 3, pp. 172–181, 2019.